Check for updates

Earthquake Engineering & Structural Dynamics

WILEY

RESEARCH ARTICLE

Modeling and Response of a Three-Story Steel Building With Sliding Slabs in Earthquake Motions

Alvaro Córdova[1] | Chung-Che Chou[1] | Chi-Jeng Wu[1] | Georgios Tsampras[2] | Chia-Ming Uang[2] | Shih-Ho Chao[3]

[1]Dept. of Civil Engineering, National Taiwan University, Taipei City, Taiwan | [2]Dept. of Structural Engineering, University of California, San Diego, USA | [3]Dept. of Civil Engineering, University of Texas, Arlington, USA

Correspondence: Chung-Che Chou (cechou@ntu.edu.tw)

Received: 27 August 2024 | **Revised:** 20 December 2024 | **Accepted:** 21 December 2024

Funding: This work was funded by the National Science and Technology Council under the project number MOST 111-2625-M-002-006, Taiwan and the 2022 Innovative Project of National Applied Research Laboratories.

Keywords: buckling-restrained brace | numerical analysis | shake table test | sliding slab

ABSTRACT

In conventional steel building construction, the slabs are rigidly connected to the beams by steel-headed stud anchors. This study explores a novel sliding slab system where the slabs are allowed to slide with respect to the steel frame by adding low-friction Teflon pads and a horizontal all-steel sandwiched buckling-restrained brace (H-SBRB) to enhance the seismic response of the building system. In this work, the effectiveness of this system in enhancing the seismic response is evaluated by constructing and validating a numerical model of a full-scale three-story steel dual-frame building equipped with a buckling restrained braced frame (BRBF). The frame specimen was subjected to strong ground motions simulated using a shaking table at the National Center for Research on Earthquake Engineering in Tainan, Taiwan. A component test of the Teflon was conducted, where the frictional behavior displayed a velocity-dependence, and the results were integrated into the analytical model. The model showed a good correlation with the test results, particularly in drift response, slab response, floor acceleration, and overall sliding response. Two H-SBRB design forces, referred to as Design 1 and Design 2, were presented, and the slab sliding response was obtained by conducting nonlinear response history analyses. Design 1 reduced the floor accelerations by 19%, the interstory drifts by 15%, and the total base shear by 13% compared to a building model with rigidly-connected slabs. In Design 2, the H-SBRB design force was reduced, leading to a reduction in floor acceleration by 31% and interstory drift by 34%.

1 | Introduction

In conventional steel building construction, the slab is rigidly connected to the beams. However, introducing a sliding slab system can enhance the seismic performance by reducing the force demand. Previous research has explored single- and multi-story isolation to protect nonstructural equipment and minimize the overall seismic response. Liu and Warn [1] conducted numerical studies on floor isolation for sensitive equipment in steel plate shear wall buildings, demonstrating significant acceleration reductions on isolated floors, but also posing a challenge in accommodating large displacement. Similarly, Cui et al. [2] conducted a shake table case study of an isolated floor system with bidirectional self-centering springs and integrated the results into a numerical model for further parametric studies. The isolation system was effective in mitigating the floor acceleration response in six ground motions. Xiang and Koetaka [3] examined the response of a two-story moment frame with isolation on the first floor using laminated viscoelastic materials (LVEM). Their numerical analysis and shake table tests highlighted substantial

© 2024 John Wiley & Sons Ltd.

mitigation of frame drifts. Further advancements were made by Xiang et al. [4] in the study of floor isolation employing LVEM between slabs and beams, which enhanced model calibration for drift prediction. Anajai and Medina [5] investigated a design procedure for a 20-story building with multi-floor isolation, where the isolated slabs functioned as a multi-tuned mass damper (TMD) system, effectively minimizing drift response. Casagrande et al. [6] explored floor isolation to protect sensitive equipment and used the isolated floors as resonant masses with shape-memory alloys and visco-elastomeric dampers. By combining experimental tests and one-dimensional numerical simulations, their work showed significant reductions in stress, deformation, and acceleration. Moreover, Villaverde [7] presented a numerical model of a 13-story building with an isolated roof using flexible bearings and viscous dampers acting as a resonant mass. This approach proved effective in reducing damage to structural and nonstructural components. Subsequent studies by Villaverde et al. [8] employed oval-shaped steel dampers in roof isolation, validating their effectiveness in reducing seismic response through both experimental and analytical methods.

Other solutions to mitigate the response of buildings have been explored, involving a force-limiting connection between the gravity and lateral system, as opposed to a rigid connection in traditional buildings. This concept was first explored by Kelly et al. [9] and Skinner et al. [10], who tested energy absorption devices in reinforced concrete structures. Tsampras et al. [11] provided a literature review and introduced the development of the physical embodiment of force-limiting deformable connections that can be used to transfer the seismic-induced horizontal inertial forces between gravity load-resisting systems and seismic force-resisting systems. Numerical studies of a 12-story reinforced concrete building [11] and a nine-story steel rocking braced frame building [12] revealed buckling restrained braces or friction devices along with low-damping rubber bearings as viable options to be used as force-limiting deformable connections. Tsampras et al. [13, 14] conducted experimental and numerical studies on force-limiting deformable connections composed of a buckling-restrained brace or friction devices and low-damping rubber bearings. Further work by Zhang et al. [15] includes shake table tests on a half-scale, four-story reinforced concrete shear wall building equipped with deformable connections, revealing the potential to reduce damage to the primary structural and non-structural components. More recent studies by Paronesso and Lignos [16] have incorporated analytical work to evaluate the effectiveness of sliding friction dampers and low-damping rubber bearings in steel concentrically braced frames, where the reduction in floor accelerations and drifts was noteworthy.

In this work, a numerical model was constructed and validated using the experimental results of shake table tests on a full-scale, three-story steel dual-frame building equipped with a buckling-restrained braced frame (BRBF) [17]. The test program was conducted in two phases. In Phase 1, the slab was allowed to slide with respect to the steel frame by using low-friction Teflon pads and a horizontal all-steel sandwiched buckling-restrained brace (H-SBRB). In Phase 2, the slab was rigidly connected to the steel frame. By using a BRB, this system has the potential of minimizing the relative displacement between the isolated slab and frame, preventing potential problems caused by large displacement that may occur in typical isolation systems. The flexibility of rubber bearings can lead to excessive relative movement between the isolated floor and the structural frame, requiring strict detailing to accommodate the displacement and prevent pounding. In contrast, the high elastic stiffness of the BRB can limit the displacement at low-to-moderate seismic events. Furthermore, the well-defined yield point can help control inertial force, while the stable post-elastic stiffness of BRB helps prevent excessive displacement. The main objectives of the research were to (1) perform a correlation between the analytical 3D model and the experimental results; (2) assess the sliding slab system's effectiveness in mitigating the seismic response by comparing it to a model with rigidly-connected slab; and (3) validate the H-SBRB design forces through nonlinear response history analyses in multiple ground motions. The numerical analyses focus on the sliding behavior during Phase 1, specifically test 5, which is approximately equal to the DBE level (PGA = 0.34 g), and test 7 (PGA = 0.62 g), which is approximately equal to 1.4 times the MCE level (PGA = 0.44 g).

TABLE 1 | Column and beam sections.

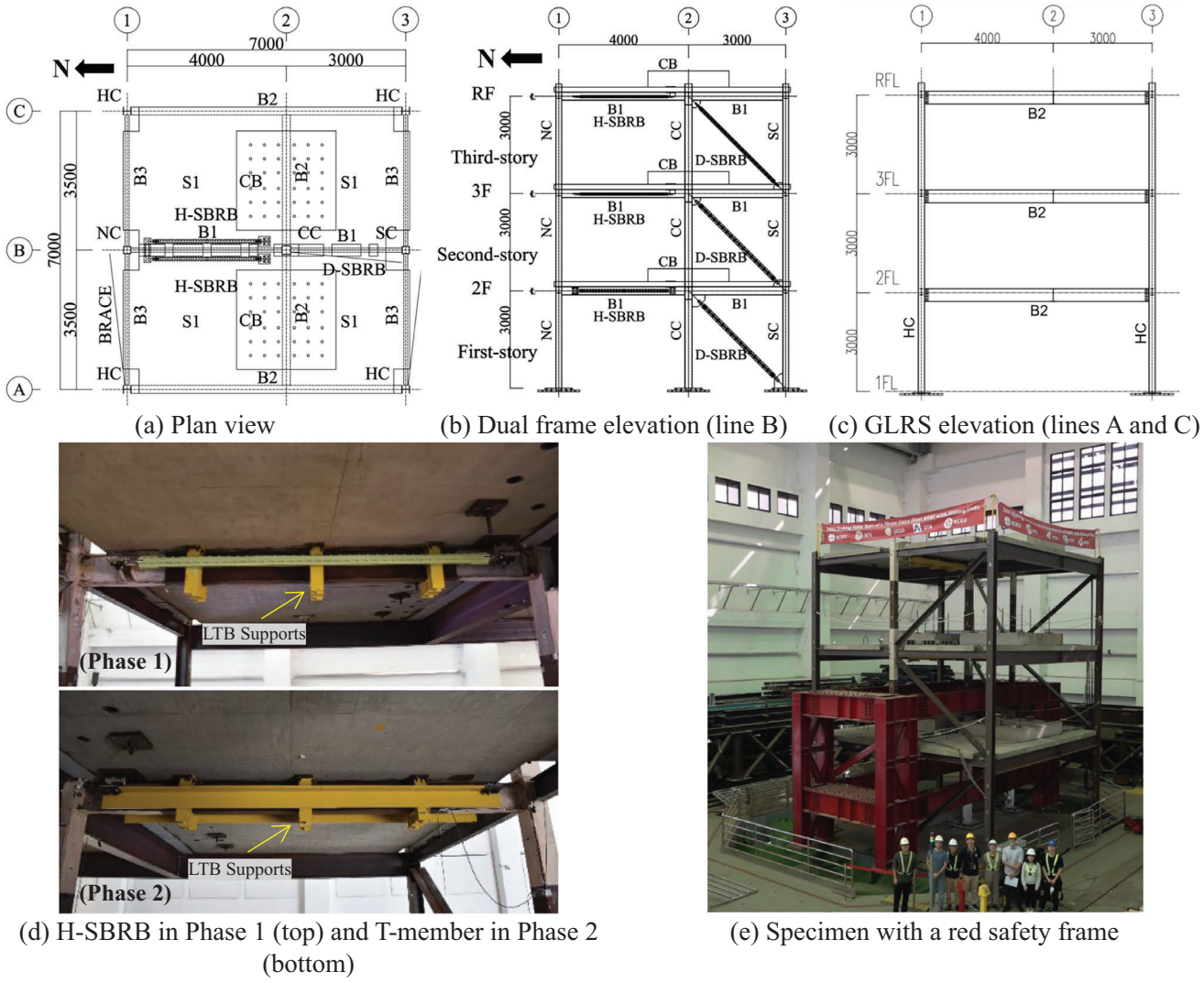
ID	Section (mm)	Type	Location
NC (North)	185 × 185 × 8	Box column	LFRS
CC (Center)	225 × 225 × 10		
SC (South)	185 × 185 × 8		
HC	200 × 200 × 8 × 12	H column	GLRS
B1	257 × 102 × 6 × 9	H beam	LFRS
B2	400 × 200 × 8 × 13		GLRS
B3	200 × 100 × 5.5 × 8		

2 | Three-Story Frame Specimen

2.1 | Steel Dual Frame Specimen

The specimen is a three-story steel dual-frame building composed of a steel special moment frame (SMF), a BRBF, and a gravity load-resisting system (GLRS). As shown in Figure 1A,B, the dual frame is positioned in the center bay, line B, and the GLRS is in the perimeter of the building, in lines A and C (Figure 1C). The SMF is composed of rolled wide-flange beams and built-up box columns, while the BRBF uses a type of steel-only sandwiched buckling-restrained braces (SBRBs). The SBRB consisted of two restraining components that sandwich the core plate with fully tensioned bolts to prevent core buckling [18]. Table 1 lists all the member sections. The beam-to-column connections and column bases in the GLRS were pinned using shear tabs. The beams in the LFRS were designed according to Chapter H of the AISC 360-22 [19] to address the interaction of axial load and moment, but the gravity beams in the GLRS were designed by only considering the gravity load without axial force. The steel for all members and connection plates was SN490B with a nominal yield stress of F_y = 325 MPa and an ultimate stress of F_u = 490 MPa. The total height of the specimen was 9000 mm, and the slabs were precast. Two concrete blocks labeled as "CB" in Figure 1A were attached on each floor, weighing a total of 59 kN for the second and third floors and 74 kN

10969845, 2025, 3, Downloaded from https://onlinelibrary.wiley.com/doi/10.1002/eqe.4300 by University Of California, Wiley Online Library on [07/11/2026]. See the Terms and Conditions (https://onlinelibrary.wiley.com/terms-and-conditions) on Wiley Online Library for rules of use; OA articles are governed by the applicable Creative Commons License



(a) Plan view (b) Dual frame elevation (line B) (c) GLRS elevation (lines A and C)

(d) H-SBRB in Phase 1 (top) and T-member in Phase 2 (bottom) (e) Specimen with a red safety frame

FIGURE 1 | Test specimen (unit: mm).

for the roof floor. The total floor weight was 333 kN for the bottom two floors and 335 kN for the roof. The lateral force-resisting system (LFRS) was designed for a site classified as stiff soil and was located 3.5 km from the Xinhua fault in Tainan, Taiwan. The empirical period was 0.26 s and the seismic design base shear was 238 kN. More details about the specimen design, instrumentation, and global response can be found in Chou et al. [17].

2.2 | Test Phase and Ground Motion

The shake table test was conducted in two phases. In Phase 1, H-SBRBs were installed beneath each floor to provide energy dissipation when the slab moved relative to the beams. Two H-SBRBs were installed per floor, connected to the slab at one end and to the SMF steel beam at the other end (Figure 1B,D). Teflon sheets were placed between the precast slab and beams to minimize friction. Three U-shaped steel supports were used to limit the lateral-torsional buckling (LTB) of the beams in the SMF (Figure 1D). Since no shear studs were used between the beam and the slab, the slab was allowed to slide, thereby transferring the inertial force mainly from the floor to the steel frame through the H-SBRBs. The sliding slab does not require composite beams, so the gravity beams in the GLRS are larger than those in typical building systems. However, slab sliding during a large earthquake is expected to reduce the input acceleration and inertial force on the building, leading to smaller member sections and less stringent seismic detailing requirements for the LFRS compared to a typical building system. The cost savings can offset the increased weight of the gravity beams. Additional cost savings also result from the elimination of shear studs and the costs associated with on-site installation. Further study on the impact of using non-composite beams is warranted. In Phase 2, all H-SBRBs were replaced by structural tee steel members with relatively high axial stiffness and strength to simulate a rigid connection between the slab and the frame (Figure 1D). Figure 1E shows the overall specimen.

The test was unidirectional in the north–south direction and the selected ground motion was obtained from September 18, 2022, Chihshang earthquake, recorded at the EYUL-EW station close to a collapsed three-story building [20]. Seven tests were conducted in Phase 1, and 10 were conducted in Phase 2 with increased intensity. In between each test, white noise tests were conducted

10969845, 2025, 3, Downloaded from https://onlinelibrary.wiley.com/doi/10.1002/eqe.4300 by University Of California, Wiley Online Library on [07/11/2026]. See the Terms and Conditions (https://onlinelibrary.wiley.com/terms-and-conditions) on Wiley Online Library for rules of use; OA articles are governed by the applicable Creative Commons License

with varying frequencies and peak intensity of 0.015 g to identify the fundamental structural period, which was $T_n = 0.52$ s.

2.3 | H-SBRB Design

The ASCE 7–22, Section 12.10.1 [21] provides guidance to compute the design diaphragm forces (F_{px}) for a conventional frame. This procedure requires to compute the lateral seismic forces from ASCE 7–22, Section 12.8.3 first [21]:

$$F_x = \frac{w_x h_x^k}{\sum_n^{i=1} w_i h_i^k} V \tag{1}$$

where the floor mass w_i was 298 kN for the second and third floors and 327 kN for the roof floor. The height h_i was 3000 mm for all stories, and the parameter k to account for the higher mode contribution equals 1.0 [22]. The base shear V was equal to 238 kN. The lateral seismic forces are then used as the numerator of the following equation to compute the diaphragm forces:

$$F_{px} = \frac{\sum_n^{i=x} F_i}{\sum_n^{i=x} w_i} w_{px} \tag{2}$$

In addition, Equation (2) must be larger than $0.2S_{DS}I_e w_{px}$ and smaller than $0.4S_{DS}I_e w_{px}$. These thresholds are associated with 0.5 and 1.0 times the peak ground acceleration (PGA) multiplied by the floor mass (w_{px}), respectively. The code recommends that floor accelerations should exceed at least 0.5 times the PGA. The spectral response acceleration parameter for short periods was $S_{DS} = 0.8$ g for Tainan site, and the importance factor was $I_e = 1.0$. For rigid slabs, the resulting forces are then multiplied by the system overstrength factor ($\Omega_o = 2.5$ for a dual frame system with a BRBF) to ensure that the diaphragm and its connection remain elastic during the MCE level event. A preliminary 2D model with sliding slabs in the previous work showed that multiplying these forces, F_{px}, by a factor of 1.5 (less than Ω_o) to design the H-SBRBs, could result in slab sliding at the DBE level [17]. The required design force for the H-SBRBs were 119, 147, and 165 kN at the second, third, and roof floors, respectively.

3 | Three-Story Frame Specimen Modeling

A 3D model was built for the specimen with the LFRS and GLRS, as well as the sliding mechanism in Phase 1 (Figure 2A–C) using the computer program PISA3D [23]. This section describes the model definitions and the model validation using the experimental data of test 7 in Phase 1.

3.1 | GLRS Modeling

The GLRS members were modeled using beam-column elements with linear-elastic properties. The gravity column base and beam-to-column connection were constructed using bolted shear tabs, thus negligible lateral stiffness was anticipated for the gravity frames. However, it was found in tests [17] that up to 10% of the base shear was distributed to these frames. So, a rotational spring was added at the gravity member ends to model the partially restrained connection stiffness, as shown in Figure 2C, marked with a helical spring symbol at the beam-to-column junction. First, to measure the gravity column moment, two strain gauge pairs were installed at the third location along the column height, one strain gauge on each flange, for all three floors so the strong-axis moment could be computed. In addition, two linear variable differential transducers (LVDT) were installed at the northeast column base as shown in Figure 2G to measure the displacement of each column flange with respect to the base plate. Then, the rotation was computed by dividing the sum of both displacements by the horizontal distance between the LVDTs. Figure 3A shows the moment-rotation behavior for the northeast column base. The analytical model used a linear rotational spring in the four-column bases, adopting an equivalent linear stiffness (shown in a red dashed line) of the observed nonlinear response, equal to $k_\theta = 850$ kN-m/rad.

The northeast second-floor beam connection was evaluated to assess the gravity beam-to-column connection stiffness. To measure the beam moment at the column face, the second-floor column bottom moment was added to the first-floor column top moment. Since only one beam is connected to this joint in the direction of the shaking, the result is approximately equal to the beam moment at the column face. As for the beam-to-column rotation, two LVDTs were placed, each near the top and bottom beam flanges as shown in Figure 2G, and for calculating the rotation, the displacements were added and divided by the distance between the LVDTs. Figure 3B shows the moment-rotation response at the beam-to-column connection. A rotational spring (Figure 2C) with linear properties (Figure 2F) was added at the gravity beam ends to model an equivalent stiffness of the test data, equal to $k_\theta = 1500$ kN-m/rad. In the GLRS, the column base and the beam-to-column connection show a bilinear response, as shown in Figure 3, due to bolt slippage in the bolt-bearing connection. In addition, the response shows a residual drift angle of about 0.005 rad, which was caused by the inability of the LFRS to return to the original position after the peak of the earthquake motion. The maximum moment compared to the plastic moment capacity of the column or beam, M_p, is also very small. The partially restrained stiffnesses obtained from the test were used in the model.

3.2 | LFRS Modeling

For the dual frame shown in Figure 2B, beam-column elements were used for all column members, with a lumped flexural plastic hinge at the end of every element. Beams in the SMF bay were also modeled using beam-column elements, but to model the reduced beam section (RBS), three additional beam-column elements were used at each beam end as shown in Figure 2D. The three elements had the unreduced sectional properties of the beam cross-section, which were prismatic along their lengths. The first element had a material property considering the measured yield stress, $F_y = 410$ MPa. To account for the reduced moment capacity of the RBS, the second and third element's intersecting node, which was positioned at the RBS center, had a lower yield stress of $0.7F_y$ (=290 MPa). The beam flanges and web in the BRBF bay were welded to the columns with complete joint penetration (CJP) welds, so the beam-to-column connection was assumed

10969845, 2025, 3, Downloaded from https://onlinelibrary.wiley.com/doi/10.1002/eqe.4300 by University Of California, Wiley Online Library on [07/11/2026]. See the Terms and Conditions (https://onlinelibrary.wiley.com/terms-and-conditions) on Wiley Online Library for rules of use; OA articles are governed by the applicable Creative Commons License

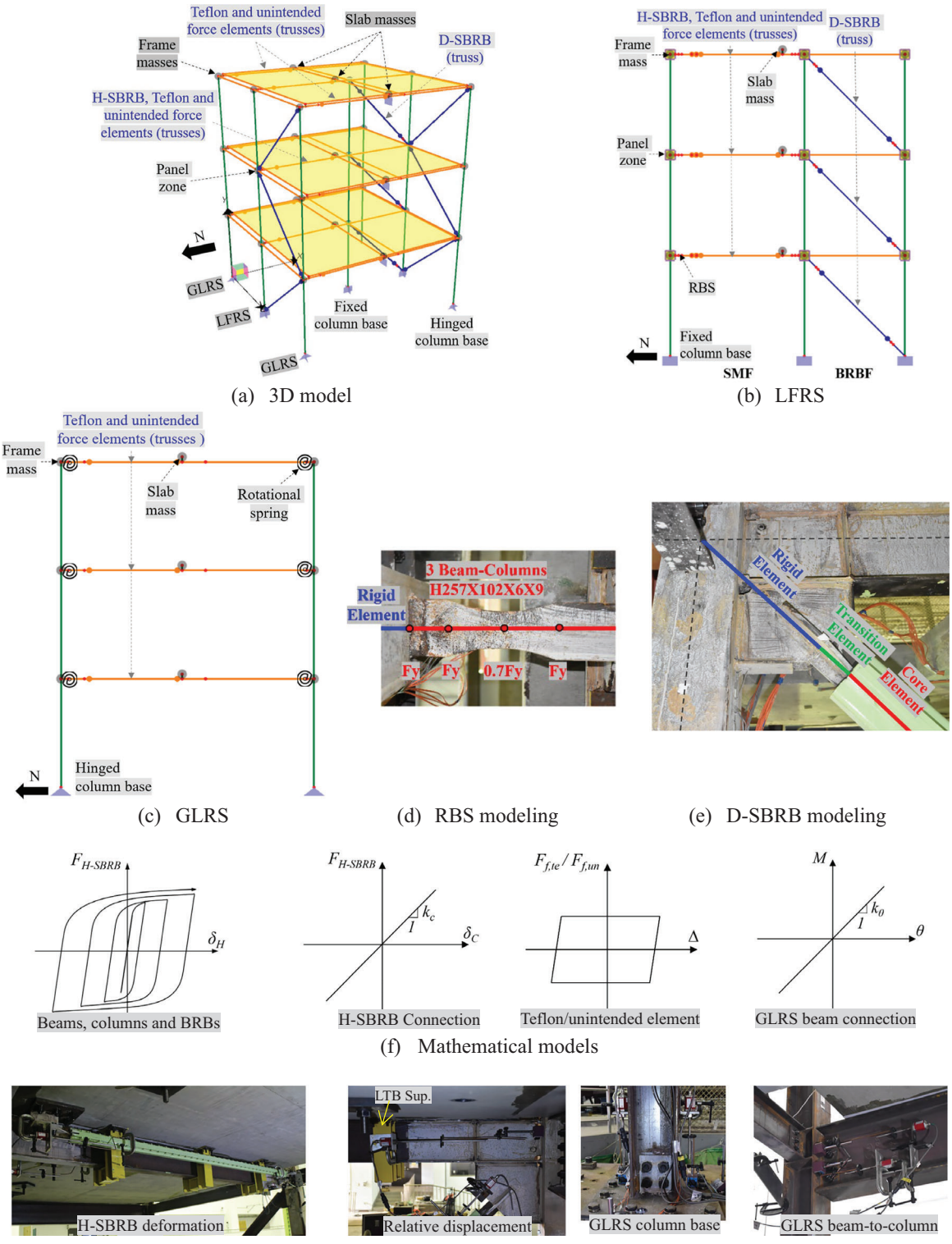


FIGURE 2 | Modeling and instrumentation of the test specimen.

rigid in the model. The SN490B steel material for all beams and columns was defined using isotropic and kinematic hardening properties experimentally validated by Chou et al. [24]. For the beam-to-column joints of the dual frame, a fully rigid zone was assigned within the panel zone. A linear-elastic rotational spring was added to account for the panel zone elastic stiffness of the built-up box column. The stiffness was computed using the following equation proposed by Krawinkler [25]:

$$k_e = \frac{Gd_b d_c t_{pz}}{(1 - d_b/H)} \tag{3}$$

where d_b is the beam depth (=257 mm), d_c is the column depth (185 mm for the north and south columns and 225 mm for the

10969845, 2025, 3, Downloaded from https://onlinelibrary.wiley.com/doi/10.1002/eqe.4300 by University Of California, Wiley Online Library on [07/11/2026]. See the Terms and Conditions (https://onlinelibrary.wiley.com/terms-and-conditions) on Wiley Online Library for rules of use; OA articles are governed by the applicable Creative Commons License

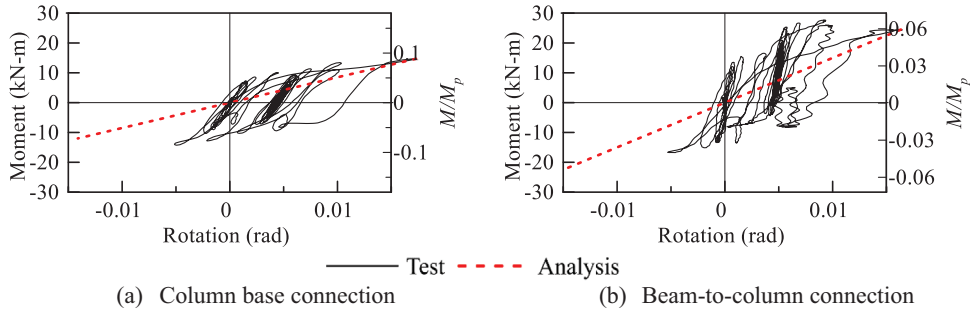


FIGURE 3 | GLRS connection stiffness in the model.

TABLE 2 | Material parameters for the modeling of H-SBRB and D-SBRB.

	E (GPa)	υ	F_{yt} (MPa)	F_{yc} (MPa)	Hsio1+	Hsio2+	Hsio1-	Hsio2-	Hkin1	Hkin2	B/Y
H-SBRB	200	0.3	325	265	0.0025	5	0.0018	3.5	0.8	24	1.1
D-SBRB	200	0.3	364	364	0.0025	5	0.0018	4.3	0.8	24	1.3

center column), t_{pz} is the panel zone thickness corresponding to twice the web plate thickness (16 mm for the north and south columns and 20 mm for the center column), G is the shear modulus (=77 GPa), and H is the distance between column inflection points from stories above and below (=3000 mm). For the north and south columns k_e = 64000 kN-m/rad, and for the center column k_e = 7296 kN-m/rad. The column base was modeled as a fixed boundary condition because it was fully CJP welded to a 60-mm thick base plate.

The diagonal SBRB (D-SBRB) was modeled using five truss elements in series as shown in Figure 2B,E. A rigid element was used at the brace end to model the column panel zone and double gusset plate connection, followed by a beam-column element to model the BRB transition section and one truss element for the BRB core. The cross-sectional area of the transition element was the average between the core and the joint, equal to 1350 mm^2 for the first and second stories and 600 mm^2 for the third story. The core element had a cross-sectional area equal to 900 mm^2 for the first and second stories and 400 mm^2 for the third story. The structural member that restrained the out-of-plane buckling of the BRB core (restraining member) was not modeled, since the BRB core showed a stable hysteretic response without strength degradation during the tests. The transition and core elements were modeled using isotropic and kinematic hardening material parameters as listed in Table 2, previously validated by Chou et al. [24]. Figure 4A shows the correlation between test and analysis for the D-SBRB at the first story for Test 7, Phase 1, and Figure 4B shows a comparison for a SBRB component test conducted according to the AISC 341-22, Chapter K3 [26].

3.3 | Modeling of Sliding Slab Mechanism

In Phase 1, the slab was allowed to move horizontally with respect to the beam. As depicted in Figure 5A, the H-SBRB is connected between the slab and the beam, and four displacement parameters were used to describe the slab sliding kinematics which includes the slab displacement, $\Delta_{s,x}$, the frame displacement, $\Delta_{f,x}$, the H-SBRB axial deformation, $\delta_{H,x}$ and the corresponding connection deformation $\delta_{C,x}$, where x corresponds to the floor level (i.e., x = 1, 2, 3). By neglecting the beam and slab axial deformation, the slab displacement is equal to the summation of the frame displacement, the H-SBRB deformation, and the deformation of its connection:

$$\Delta_{s,x} = \Delta_{f,x} + \delta_{H,x} + \delta_{C,x} \tag{4}$$

The H-SBRB deformation was measured by using two LVDTs, one at each end, connected between the H-SBRB end and the restraining element (Figure 2G), where the total deformation is the summation of the two LVDT data. The relative displacement between the slab and the frame is defined as:

$$\Delta_{r,x} = \Delta_{s,x} - \Delta_{f,x} \tag{5}$$

This displacement was directly measured using three LVDTs per floor, installed between the LTB support, rigidly connected to the slab, and the column panel zone in the dual frame (Figure 2G). By combining Equations (4) and (5), the connection deformation of the H-SBRB, is computed by subtracting the H-SBRB deformation from the relative displacement:

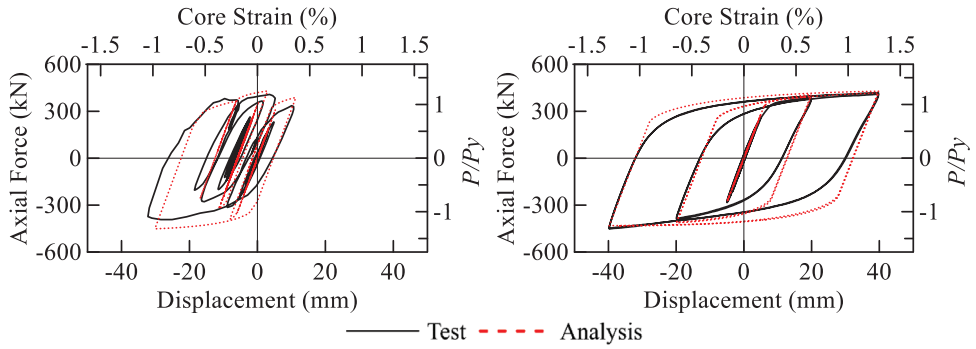
$$\delta_{c,x} = \Delta_{r,x} - \delta_{H,x} \tag{6}$$

The sliding slab force equilibrium is shown in Figure 5B, where the inertial force, F_i, is not the same as the H-SBRB force, $F_{H\text{-}SBRB}$, due to the presence of friction forces, F_f, composed by the Teflon friction force, $F_{f,te}$, and other friction forces referred to as an unintended force, $F_{f,un}$. Figure 5B shows the free body diagram, and the equilibrium equation is:

$$F_i = F_{S\text{-}HBRB} + F_{f,te} + F_{f,un} = F_{S\text{-}HBRB} + F_f \tag{7}$$

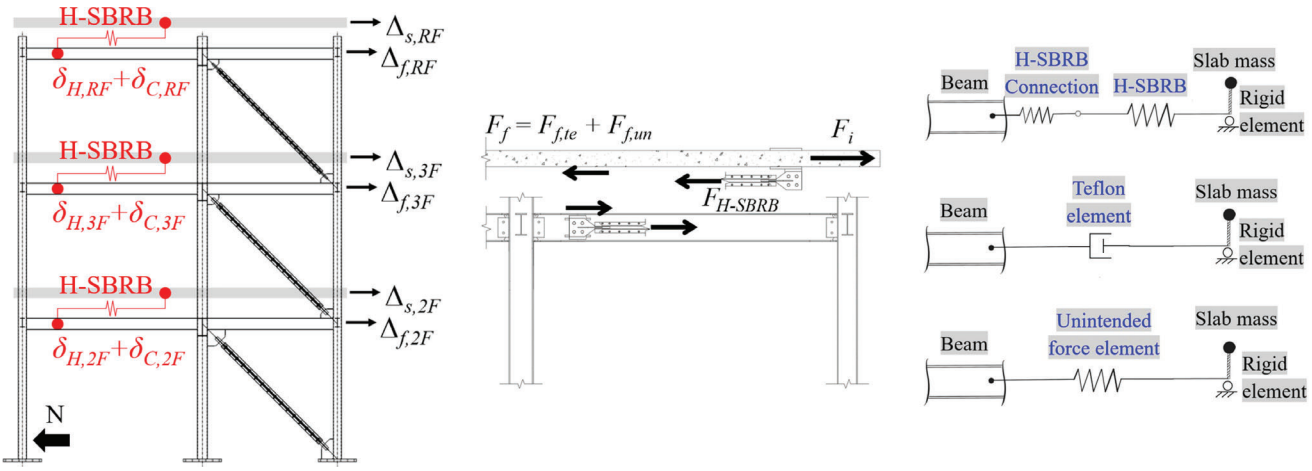
where, $F_f = F_{f,te} + F_{f,un}$.

10969845, 2025, 3, Downloaded from https://onlinelibrary.wiley.com/doi/10.1002/eqe.4300 by University Of California, Wiley Online Library on [07/11/2026]. See the Terms and Conditions (https://onlinelibrary.wiley.com/terms-and-conditions) on Wiley Online Library for rules of use; OA articles are governed by the applicable Creative Commons License



(a) Test 7, Phase 1 (b) Component test (AISC 341-22 protocol)

FIGURE 4 | Test response and model correlation of the first story D-SBRB.



(a) Displacement parameters (b) Force equilibrium (c) Sliding mechanism model

FIGURE 5 | Sliding slab mechanism.

In the PISA3D, the sliding slab mechanism was constructed using horizontal truss elements to model the forces that compose the inertial force in Equation (7). The concrete slab mass was modeled using three lumped masses per floor, one for the dual frame bay and one for each of the two gravity frame bays (Figure 2A), with the mass computed based on the corresponding tributary areas. To account for the slab center of mass offset, the slab mass was elevated 203.5 mm above the beam, associated with half of the beam depth (=128.5 mm) and half of the slab thickness (=75 mm) using a vertical rigid element (Figure 2A and Figure 4C). For the dual frame, this rigid element was connected to the beam by using three truss elements in parallel including the H-SBRB element, a Teflon element, and an unintended force element, as shown in Figure 5C. The H-SBRB element had an additional truss element in series to account for the flexibility of the H-SBRB-to-slab connection as well as the H-SBRB-to-beam connection. A bilinear damper element was used to model the Teflon friction force. A truss element was used to account for the unintended force, caused by friction between the beam flange and its LTB support, and between the slab and the side plate of the beam top flange to prevent slab in-plane torsion [17]. The same modeling scheme was used to model Teflon and unintended forces in the gravity frames (i.e., No H-SBRB element in these frames). Then, the three lumped masses were interconnected by a transverse rigid element in the east-west direction (Figure 2A) to simulate the effect of a rigid slab. The steel frame mass was defined using lumped masses at each floor as a set of seven lumped masses, one in each beam-column joint, corresponding to half of the steel members weight above and below the floor level (Figure 2A).

3.4 | H-SBRB Modeling

After conducting all shake table tests, one H-SBRB at the roof was removed from the frame specimen and tested axially in two phases as shown in Figure 6A. In Phase 1, a quasi-static test was conducted with the displacement history in test 7 (Figure 6B). In Phase 2, a quasi-static test was conducted with a displacement protocol as per AISC 341-22, Chapter K3 [26]. The test results of Phase 1 are shown in Figure 6B and those of Phase 2 in Figure 6C. Despite the H-SBRB being the same type of Sandwiched BRB used as a diagonal brace, a new material model was specifically defined and fitted for these elements due to their small size. The largest H-SBRB core at the roof is 228 mm^2, which is about 25% of the D-SBRB core at the first and second stories, equal to 900 mm^2. A material model with isotropic and kinematic properties was calibrated to fit both component tests (Figure 6B,C). In Phase 1, for the tension side, the R_y value was 1.23, obtained from a coupon test, corresponding to a measured yield stress of F_{yt} = 400 MPa, where the nominal yield stress is F_{ytn} = 325 MPa. However, in

10969845, 2025, 3, Downloaded from https://onlinelibrary.wiley.com/doi/10.1002/eqe.4300 by University Of California, Wiley Online Library on [07/11/2026]. See the Terms and Conditions (https://onlinelibrary.wiley.com/terms-and-conditions) on Wiley Online Library for rules of use; OA articles are governed by the applicable Creative Commons License

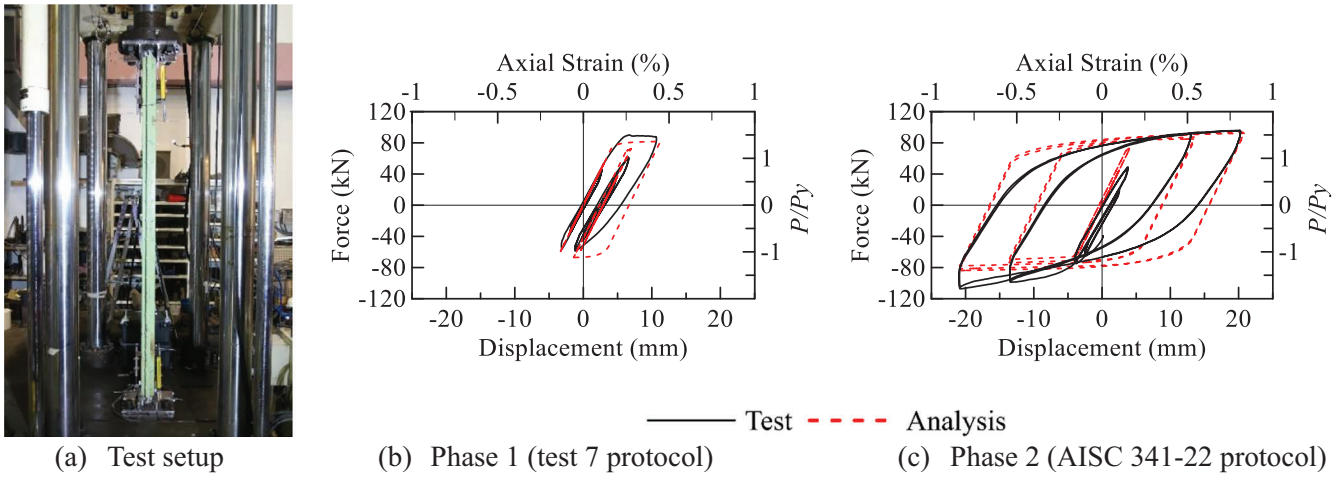


FIGURE 6 | Component tests for the roof H-SBRB.

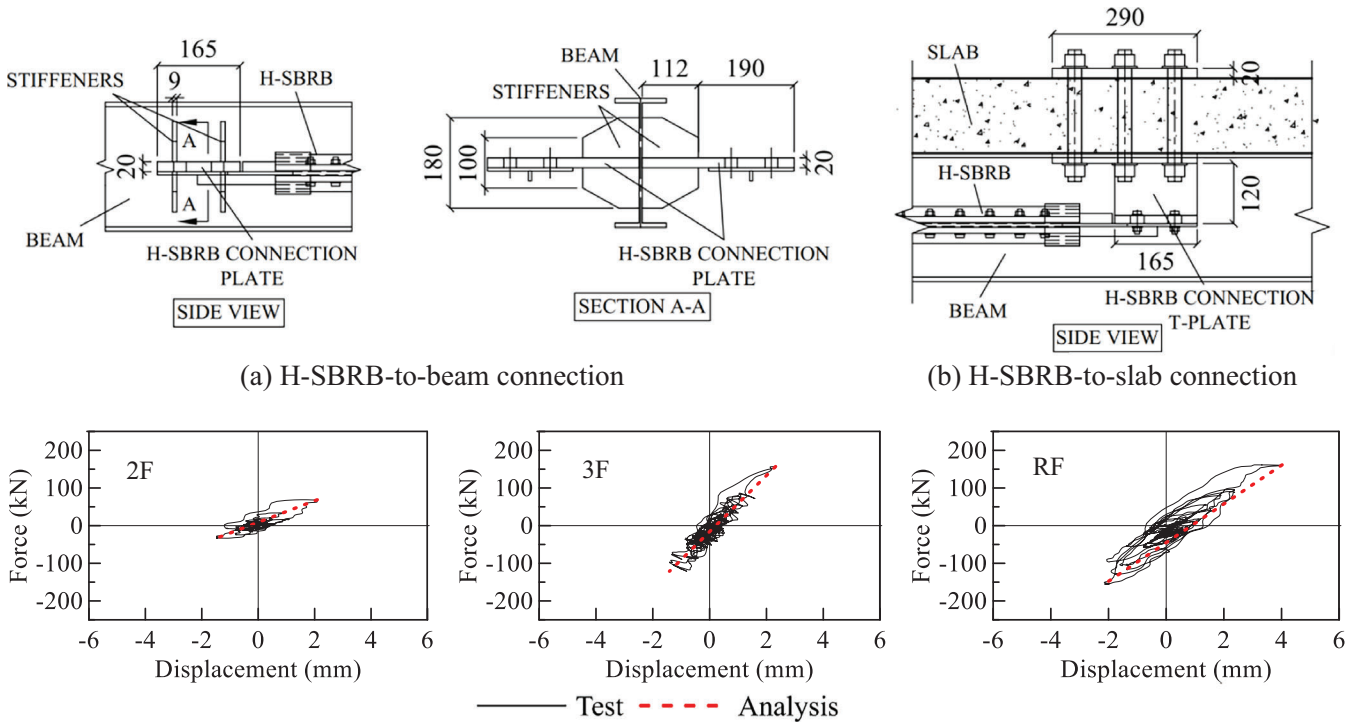
Phase 2 after reversed cycles, the yield stress was lower due to the Bauschinger effect. To account for this effect, the input yield stress had to be lower and taken as F_{yt} = 325 MPa, and a B/Y parameter was set to 1.1. The B/Y parameter refers to the bounding surface (B) corresponding to the isotropic hardening, divided by the yielding surface corresponding to the kinematic hardening (Y). A high B/Y value represents stronger isotropic hardening, while a low B/Y value emphasizes kinematic hardening, which results in the yield surface shifting rather than expanding, and allowing for the Bauschinger effect when yielding in the opposite direction. In the compression side, the Bauschinger effect was more pronounced in Phase 1 than in Phase 2 so a lower yield point of F_{yc} = 265 MPa was defined to fit both phase tests. This model did not include the effect of friction between the core and restraining member due to Poisson's or core buckling when the brace was under compression. Therefore, the model tended to slightly underestimate the compression force for displacements below −10 mm as seen in Figure 6C. Table 2 lists all parameters to model the H-SBRB. The parameters Hsio1+ and Hsio1− control the initial isotropic hardening behavior in tension and compression, respectively, influencing the rate at which the yield surface expands as the plastic deformation accumulates in the respective direction. The parameters Hsio2+ and Hsio2- govern a gradual expansion of the yield surface in tension and compression, respectively, with continued plastic deformation after multiple cycles. The parameter Hkin1 represents the initial kinematic hardening modulus, dictating the initial stiffness of the back-stress evolution and influencing yield surface shift under cyclic loading. The parameter Hkin2 defines the kinematic hardening response, accounting for nonlinearities in the shifting of the yield surface to capture cyclic behavior under high strain ranges or repeated cycles. The parameters for the D-SBRB modeling are also included in Table 2.

Figure 7A,B show the connection details of the H-SBRB to the beam and slab, respectively. The H-SBRB was connected to the beam by welding a horizontal plate to the beam web. Once the beam was erected, the H-SBRB was bolted to the connection plate. The other end of the H-SBRB was connected to the slab by using six anchor bolts. Two horizontal H-SBRBs were used per floor to avoid the weak axis bending of the beam, and to avoid in-plane slab rotation due to the eccentricity between the slab center and the H-SBRB centerline. The connections were designed using a capacity-design principle with a required axial load of $P_u = \beta\omega R_y P_y$, where β is the compression strength adjustment factor (=1.2), ω is the strain hardening factor (=1.12) and $R_y P_y$ is the expected yield axial load. By using Equation (6), a maximum connection displacement of 4 mm was detected in test 7. The displacement was caused by the bending flexibility of the connection plate and slippage in the bolt-bearing connection. The displacement could not be neglected when compared to the H-SBRB maximum displacement of 11 mm at the roof (Figure 6B). Once the connection displacement was obtained using Equation (6), the connection force was equal to that of the H-SBRB because they were in series. Figure 7C shows the force versus the connection displacement of the H-SBRB. A single truss element connected in series with the H-SBRB was used in the model, as shown in Figure 5C, to account for the flexibility of both the H-SBRB-to-slab and H-SBRB-to-beam connection. In Figure 7C, a linear interpolation was drawn to obtain the stiffness value for the linear-elastic truss elements at the three-floor levels. The stiffness values were k_c = 28.6, 74.5, and 51.4 kN/mm for the second, third, and roof floors, respectively. The effective stiffness of these two elements in series was also computed and compared to the H-SBRB elastic stiffness reducing the elastic stiffness of H-SBRB by 25%. This can be critical for the initial distribution of the inertial force, particularly considering the Teflon and unintended frictions which may delay the sliding initiation.

3.5 | Friction Force Response

Figure 8A presents the response of the inertial force versus the relative displacement in tests 5 and 7 (represented by a solid blue line), corresponding to the DBE and 1.4MCE intensities, respectively. To obtain the inertial force, four accelerometers were used on top of each floor slab and then multiplying the average floor acceleration by the concrete floor mass. The H-SBRB hysteresis is also plotted but with respect to the axial deformation (represented by an orange dashed line). The force of H-SBRB was computed based on the elastic stiffness and the deformation at all floors in Test 5, and at the second floor in Test 7, where the deformation did not exceed the yield displacement (=4 mm). The elastic stiffness of H-SBRB, $k_{H\text{-}SBRB}$, was computed using

10969845, 2025, 3, Downloaded from https://onlinelibrary.wiley.com/doi/10.1002/eqe.4300 by University Of California, Wiley Online Library on [07/11/2026]. See the Terms and Conditions (https://onlinelibrary.wiley.com/terms-and-conditions) on Wiley Online Library for rules of use; OA articles are governed by the applicable Creative Commons License



(a) H-SBRB-to-beam connection

(b) H-SBRB-to-slab connection

(c) H-SBRB connection force vs. displacement ($F_{H\text{-}SBRB}$ vs. $\delta_{C,x}$)

FIGURE 7 | H-SBRB connection.

Equation (8), where k_j is the axial stiffness of the joint, k_t is the axial stiffness of the transition zone, and k_c is the axial stiffness of the core. In Test 7, the H-SBRB exceeded the elastic limit at both the roof and the third floor. The force in the roof H-SBRB was directly obtained from its component test, as illustrated in Figure 6B. To determine the force of the third-floor H-SBRB, a numerical model was developed in PISA3D with the fitted material parameters obtained from the correlation for the roof H-SBRB, as shown in Figure 6B,C, and applying the deformation history recorded at the third floor in Test 7.

$$k_{H\text{-}SBRB} = \frac{1}{\frac{1}{k_j} + \frac{1}{k_t} + \frac{1}{k_c}} \tag{8}$$

The relative displacement, $\Delta_{r,x}$, is larger than the H-SBRB deformation, $\delta_{H,x}$, due to the flexibility of the connection, as shown in Figure 7C and as expressed in Equation (6). This difference is clear in Figure 8A where the relative displacement of the inertial force response (shown in blue line) is larger than that of the H-SBRB response (shown in orange line). To obtain the friction force, F_f, the H-SBRB force is subtracted from the inertial force (Equation 7). This force is then plotted with respect to the relative displacement as shown in Figure 8B displaying a frictional-type response. The total friction force was caused by the Teflon friction force and other sources referred to as unintended forces mainly caused by friction between the beam flange and its LTB support, and between the slab and the side plate on the beam top flange in the GLRS to prevent slab torsion [17]. Since the unintended forces were very difficult to quantify, the Teflon friction force was verified by conducting a component Teflon test and used to solve for the unintended force by Equation (7).

3.6 | Teflon Force and Unintended Force Modeling

The Teflon had a friction coefficient of 6.3%, obtained from a quasi-static test of a one-story subassemblage with a sliding slab where the sliding velocity ranged between 0.5 and 1 mm/s [27]. In this work, the Teflon force was obtained from a post-earthquake component test with the pressure, displacement, and velocity conditions as obtained from the shake table test. Then, the unintended force can be found based on Equation (7).

Figure 9A shows a sketch of a friction-based connection developed at UC San Diego for a shake table test conducted in 2023 in Tainan, Taiwan. One of the friction-based connections that was used in the shake table test [28] was reused in this research to assess the frictional behavior of Teflon-steel interface, similar to the friction interfaces between the Teflon at the bottom of the sliding slab and the top flange of steel beams. A normal force was applied to simulate the normal pressure on the Teflon-steel contact pressure expected in the shake table test. Figure 9B shows the test setup, where the connection was fixed on the left-hand side including a 500 kN-capacity load cell to measure the total force. The end on the right-hand side was rigidly connected to the actuator. A bolt load cell was used to monitor the bolt tension force of 8 kN, corresponding to a pressure of 500 MPa close to the maximum Teflon pressure on the roof floor in the shake table test. Figure 10A shows the bolt tension history in four different velocity tests, where the time was normalized with respect to the final test time in different test durations. The bolt tension was nearly constant in all tests. Two LVDTs were positioned between the sliding plate and the steel channel, one on each side. Four tests were conducted with a constant

10969845, 2025, 3, Downloaded from https://onlinelibrary.wiley.com/doi/10.1002/eqe.4300 by University Of California, Wiley Online Library on [07/11/2026]. See the Terms and Conditions (https://onlinelibrary.wiley.com/terms-and-conditions) on Wiley Online Library for rules of use; OA articles are governed by the applicable Creative Commons License

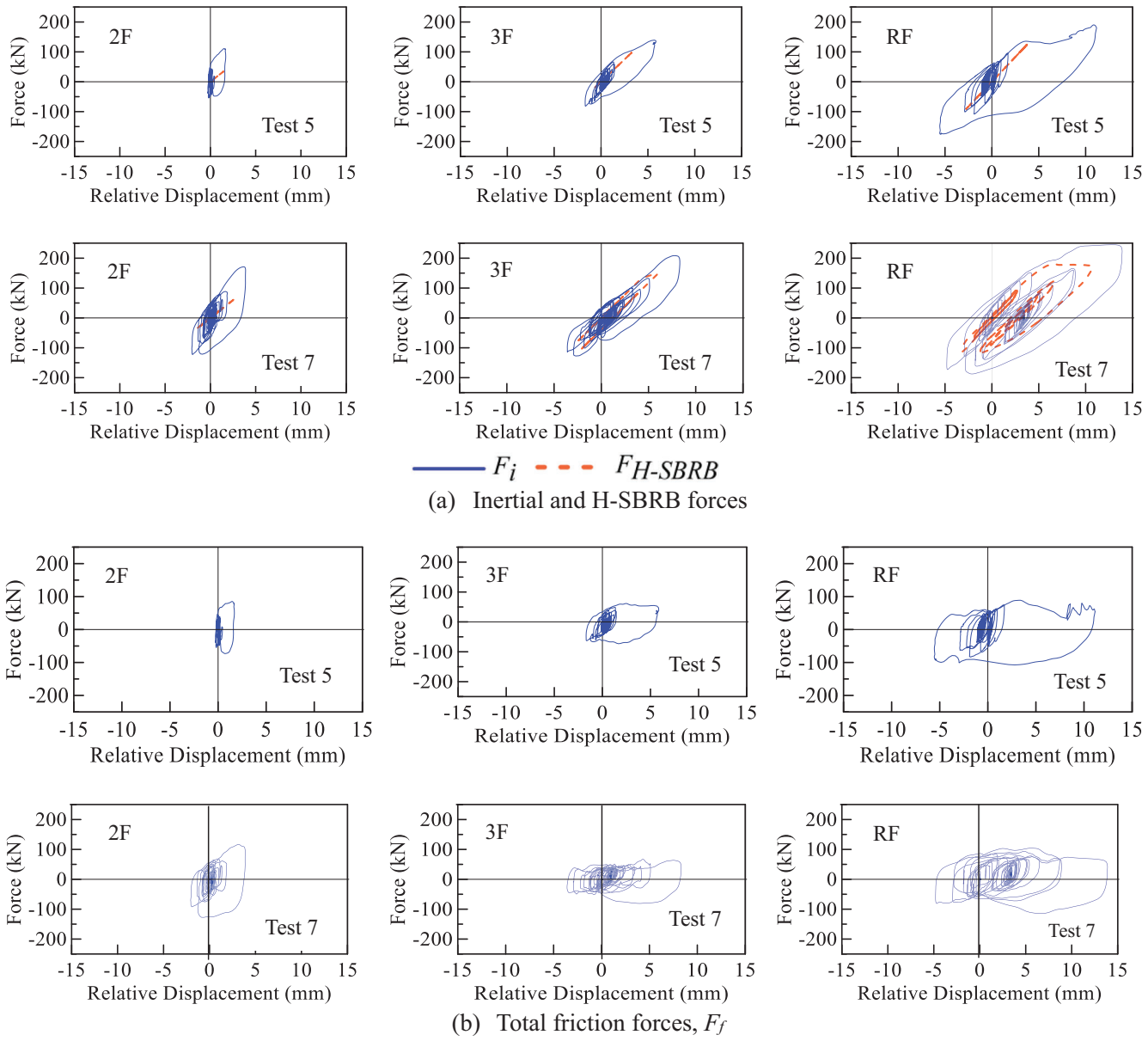
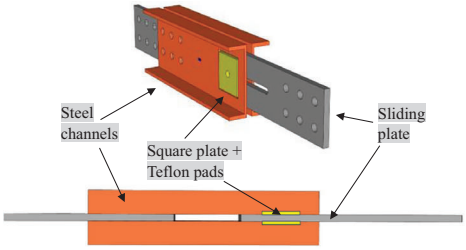


FIGURE 8 | Hysteresis of inertial, H-SBRB, and total friction forces for tests 5 and 7.

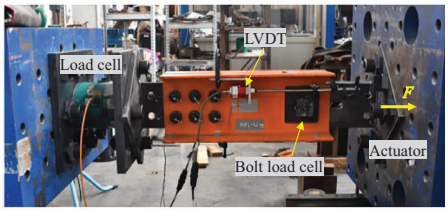
actuator velocity of 10, 125, 250, and 500 mm/s, to obtain the velocity-dependent friction response. The peak relative velocities of the floor in the shake table test (test 7) were 90, 127, and 142 mm/s at the second, third, and roof floors so the actual friction coefficient values could be linearly interpolated from the Teflon component test results (Figure 9). The test displacement protocol had two peak displacement values, 35 and 70 mm, to capture possible displacement dependence; two full cycles were conducted at each displacement amplitude (Figure 10B and Table 3). These displacements were beyond the peak roof relative displacement of 14 mm in the shake table test (test 7). The resulting friction coefficient was computed based on the free body diagram shown in Figure 9C by considering two contact surfaces. The Teflon pads before and after testing are shown in Figure 9D. Figure 10C–F shows the test results from which four different friction coefficients were obtained corresponding to each of the four testing velocities. Table 3 summarizes the test protocol and results. These coefficients are plotted with respect to velocity as shown in Figure 10G. Figure 10H shows the friction coefficient-displacement relation for the four constant velocities in the Teflon tests.

The test revealed that the Teflon friction coefficient was velocity-dependent, consistent with past research on Teflon sliding against a steel surface [29, 30]. Therefore, to obtain the actual shake table Teflon forces, the relative velocities were first computed. The relative displacement data were directly measured using LVDTs placed between the slab and the frame, and then, differentiated with respect to time to obtain the relative velocity. Figure 11A,B show the relative displacement and velocity histories at the roof floor during test 7. By using a trilinear relationship in Figure 10G, the friction coefficient for different relative velocities at each floor could be computed. The friction coefficient was then multiplied by the slab weight to obtain the Teflon force where the peak values were 40, 45, and 51 kN at the second, third, and roof floors, respectively. The ratio between the peak Teflon force and the

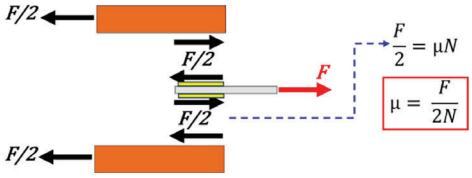
10969845, 2025, 3, Downloaded from https://onlinelibrary.wiley.com/doi/10.1002/eqe.4300 by University Of California, Wiley Online Library on [07/11/2026]. See the Terms and Conditions (https://onlinelibrary.wiley.com/terms-and-conditions) on Wiley Online Library for rules of use; OA articles are governed by the applicable Creative Commons License



(a) 3D and top view



(b) Test setup and instrumentation



(c) Free body diagram (top view)



(d) Teflon pads before (left) and after (right) tests

FIGURE 9 | Component test of Teflon.

TABLE 3 | Teflon test protocol and results.

Test number	Number of cycles per test	Peak displacement (mm)	Constant velocity (mm/s)	Friction coefficient
1	2	35	10	0.1
		70		
2		35	125	0.15
		70		
3		35	250	0.2
		70		
4		35	500	0.2
		70		

peak inertial force was 0.23, 0.22, and 0.21 at the second, third, and roof floors, respectively. Figure 12 shows the Teflon friction force versus relative velocity at each floor, and the largest velocity occurs at the roof resulting in a larger Teflon force.

The modeling of Teflon required a velocity-dependent element positioned horizontally as shown in Figure 5C with bilinear properties available in the PISA3D computer program. The element requires three parameters, F_r, the primary slope force limit and *C1* and *C2*, the first and second slope coefficients. These properties were fitted to match the velocity-dependent path of the Teflon component test as shown in Figure 13A. The element could model the response up to a velocity of ±250 mm/s. However, the peak relative velocities computed from the shake table test were 90, 127, and 142 mm/s at the second, third, and roof floor, respectively, below the 250 mm/s limit so the damper element could effectively model the Teflon friction response. Figure 13B shows the Teflon friction coefficient versus the displacement for the three floors in test 7.

Figure 14A shows the actual Teflon force history at the roof together with the total friction force history obtained from the test. The difference between them corresponds to the unintended force as shown in Figure 14B. The hysteresis responses of both the Teflon and unintended force is shown in Figure 14C,D. The Teflon force–displacement relation shows a force-growing path, as the velocity increases over time that is different from a traditional Coulomb friction model. Although the Teflon force is a large source of the total friction force during the slab sliding mechanism, the remaining unintended force is still large as shown in Figure 14D. In test 7, the peak unintended force at the roof floor was 83 kN, which is a large value when compared to the peak inertial floor force of 245 kN. Likewise, the peak unintended forces were 118 and 51 kN at the second and third floors, compared to the peak inertial floor forces of 171 and 208 kN, respectively. As expected, the second floor experienced the lowest inertial force, but in this floor, the Teflon force was also the lowest due to a small relative velocity (Figure 12) and the HBRB did not yield (Figure 8A). In general, this result showed that the unintended force could not be neglected and needed to be accounted for in a computer model.

The unintended force at the roof as shown in Figure 14D displays a complex behavior within the first 5 mm, then becomes a flat response as the slab slides beyond this value. To model this behavior, a Coulomb friction model was adopted. However, instead

10969845, 2025, 3, Downloaded from https://onlinelibrary.wiley.com/doi/10.1002/eqe.4300 by University Of California, Wiley Online Library on [07/11/2026]. See the Terms and Conditions (https://onlinelibrary.wiley.com/terms-and-conditions) on Wiley Online Library for rules of use; OA articles are governed by the applicable Creative Commons License

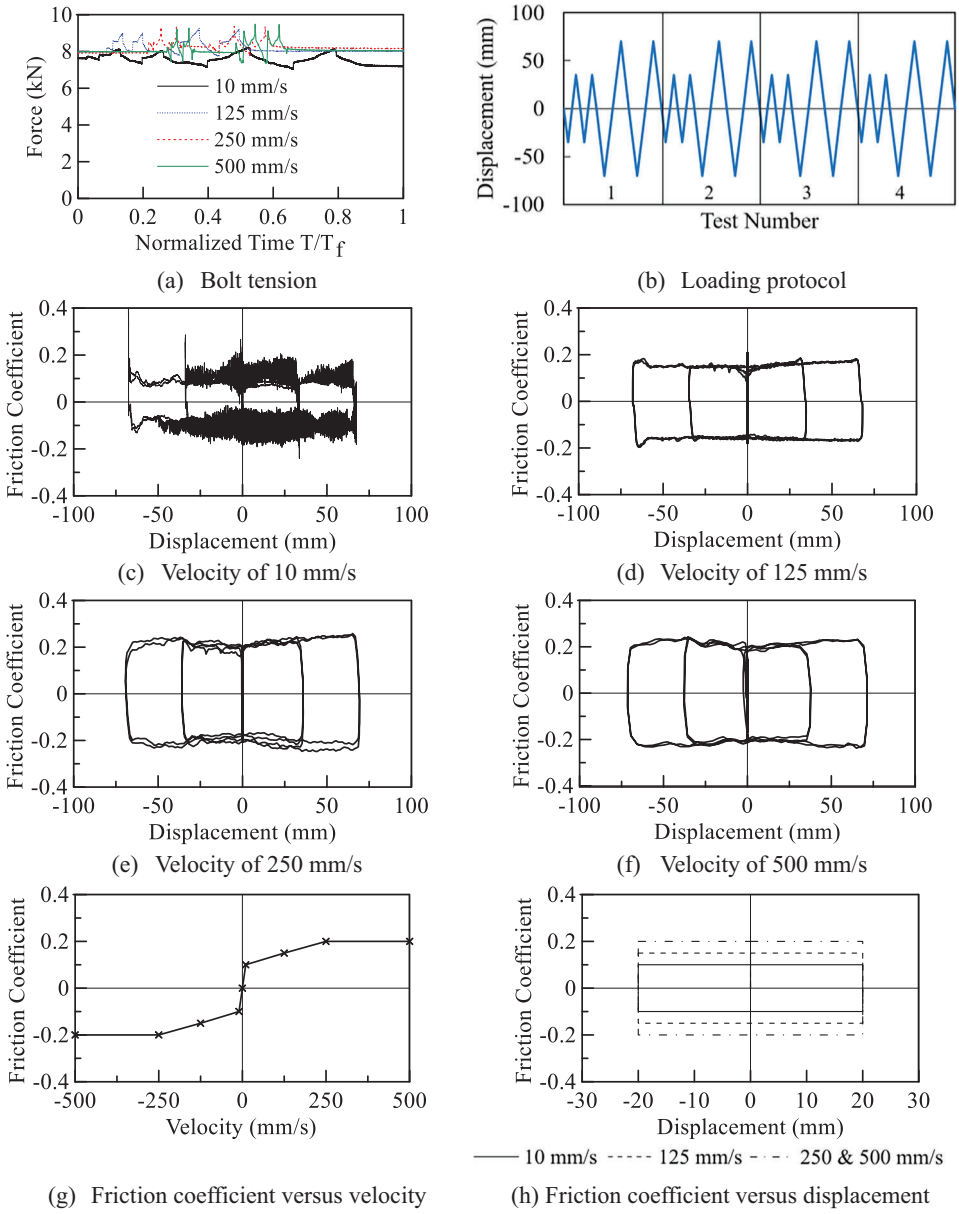


FIGURE 10 | Bolt load history, loading protocol, and test results for the Teflon component.

of a rigid initial slope, a high stiffness value of $E = 2000$ GPa was used which is 10 times the steel elastic modulus, to avoid high-frequency responses as proposed by Constantinou et al. [31]. The force plateau was set to 30 kN at all floors, which approximately matched the sliding plateau at the third and roof floors, as shown in Figure 14D. However, the second floor experienced a larger unintended force, so an additional truss element with a stiffness of 21 kN/mm was added in parallel. The unintended force sources identified in Section 3.5 can be significantly reduced by eliminating the lateral support and the side plate. For comparison, Figure 15A shows the Teflon hysteresis response using the friction coefficient of 6.3% in the analysis, found in [27] for a maximum test velocity of 1 mm/s, and Figure 15B shows the corresponding unintended force. This Teflon force is half of the Teflon force found in the component test shown in Figure 14C, highlighting the importance of considering the velocity-dependent characteristics of Teflon.

3.7 | Comparison Between Analysis and Test

Once the 3D model was built, a modal analysis was run with damping ratios of 2% for the first two modes and then the Rayleigh method was used to compute the damping matrix. The selected damping ratio of 2% was based on a companion study by Huang et al. [33], which reported damping ratios ranging from 1% to 5% in low-vibration tests. The fundamental structural period was $T_n = 0.54$ s, close to that of the actual specimen equal to 0.52 s [17]. Then, to further validate the 3D model, a nonlinear response-history analysis (NRHA) was run with the measured shake table motions from test 1 to test 7. Figure 16 shows the roof drift response for all motions in sequence. For comparison between test and analysis results, the difference in absolute peak values during large motions (e.g., Tests 5–7) was about 7%. Moreover, only the results of test 7 are compared with the analysis shown in Figures 17 and 18.

10969845, 2025, 3, Downloaded from https://onlinelibrary.wiley.com/doi/10.1002/eqe.4300 by University Of California, Wiley Online Library on [07/11/2026]. See the Terms and Conditions (https://onlinelibrary.wiley.com/terms-and-conditions) on Wiley Online Library for rules of use; OA articles are governed by the applicable Creative Commons License

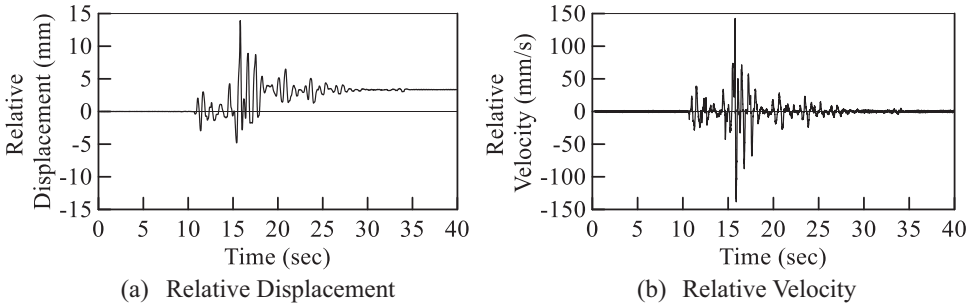


FIGURE 11 | Roof relative displacement and velocity (Test 7).

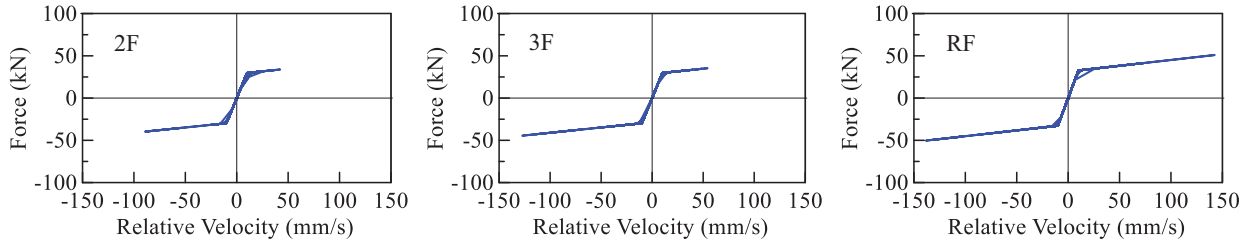


FIGURE 12 | Teflon force at each floor during shake table test (Test 7).

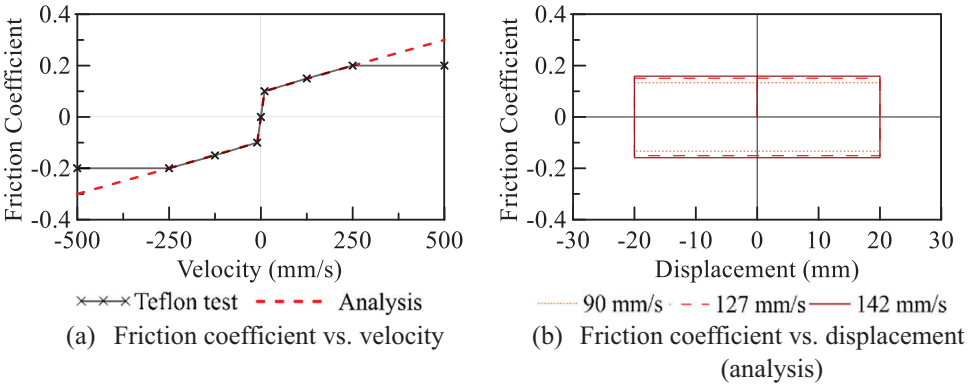


FIGURE 13 | Teflon frictional behavior.

Figures 17A,B compare frame displacements and slab displacements between the analysis and test results. The peak frame displacements in test 7 are 51, 108, and 142 mm while the analysis results showed 49, 99, and 130 mm at the second, third, and roof floors. The peak slab displacements in test 7 are 62, 118, and 157 mm while the analysis results showed 53, 106, and 138 mm at the second, third, and roof floors. Figure 17C shows the floor acceleration results where the test peak values are 0.57, 0.7, and 0.75 g while the analysis showed 0.65, 0.68, and 0.71 g at the second, third, and roof floors. Figure 18A shows the Teflon hysteresis response and Figure 18B shows the H-SBRB response. Finally, the global sliding slab response is shown in Figure 18C where the floor inertial force is plotted with respect to the relative displacement. In general, the analysis history responses closely match the test results. This comparison is important to validate the model accuracy and study the three-story frame in different ground motions.

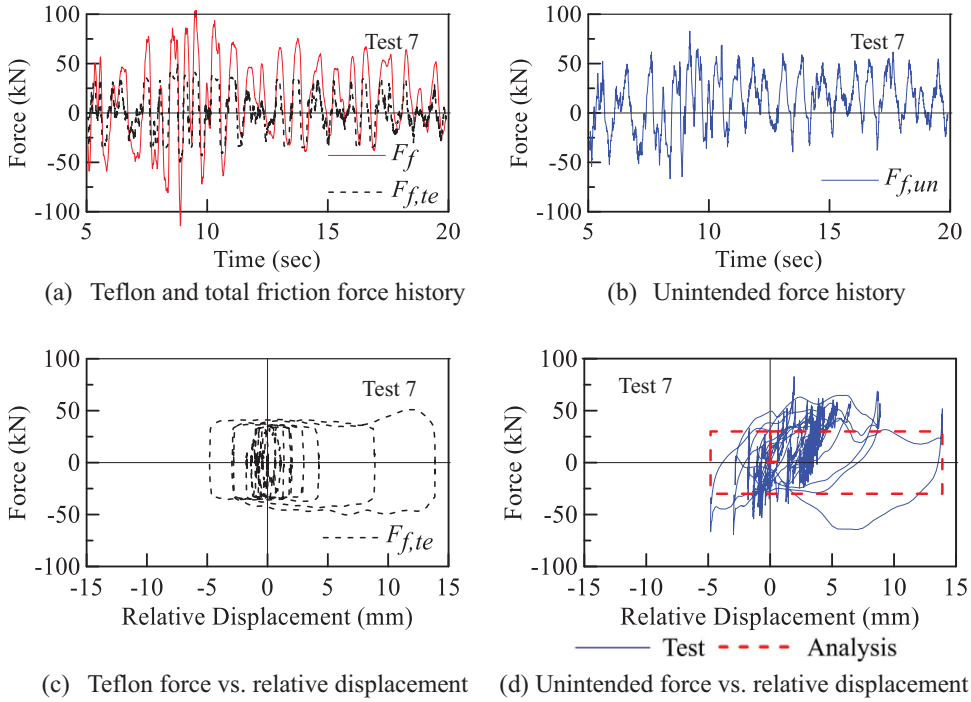
The linear model prediction representing the GLRS connection stiffness presented in Section 3.1, showed an error of about 10% when comparing the peak values of test results to analysis results, as shown in Figure 17 for the frame and slab displacement and floor acceleration. Figure 18 also shows a similar prediction error for the Teflon force, HBRB force, and global force response.

4 | Nonlinear Response-History Analyses of The Three-Story Frame With Sliding Slabs

4.1 | Scaling of Ground Motions

Given the near-fault nature of the Chihshang motion, 11 near-fault motions were selected for the nonlinear response time analyses of the three-story frame specimen at the DBE and MCE levels. The objective was to validate the design procedure of

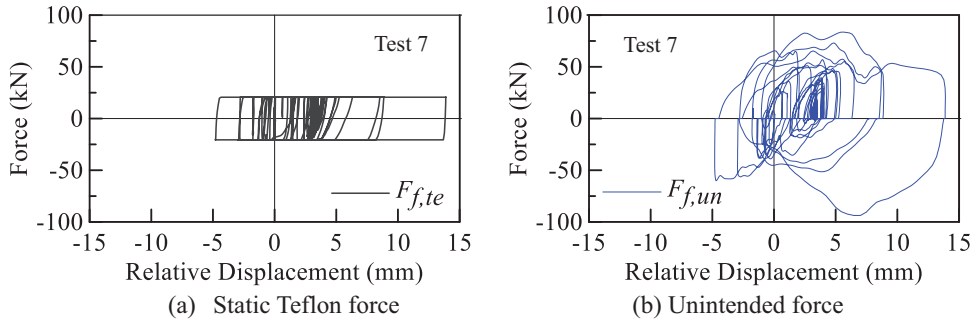
10969845, 2025, 3, Downloaded from https://onlinelibrary.wiley.com/doi/10.1002/eqe.4300 by University Of California, Wiley Online Library on [07/11/2026]. See the Terms and Conditions (https://onlinelibrary.wiley.com/terms-and-conditions) on Wiley Online Library for rules of use; OA articles are governed by the applicable Creative Commons License



(a) Teflon and total friction force history (b) Unintended force history

(c) Teflon force vs. relative displacement (d) Unintended force vs. relative displacement

FIGURE 14 | Teflon and unintended force behavior at the roof floor.



(a) Static Teflon force (b) Unintended force

FIGURE 15 | Teflon and unintended force behavior at the roof floor using a friction coefficient of 6.3%.

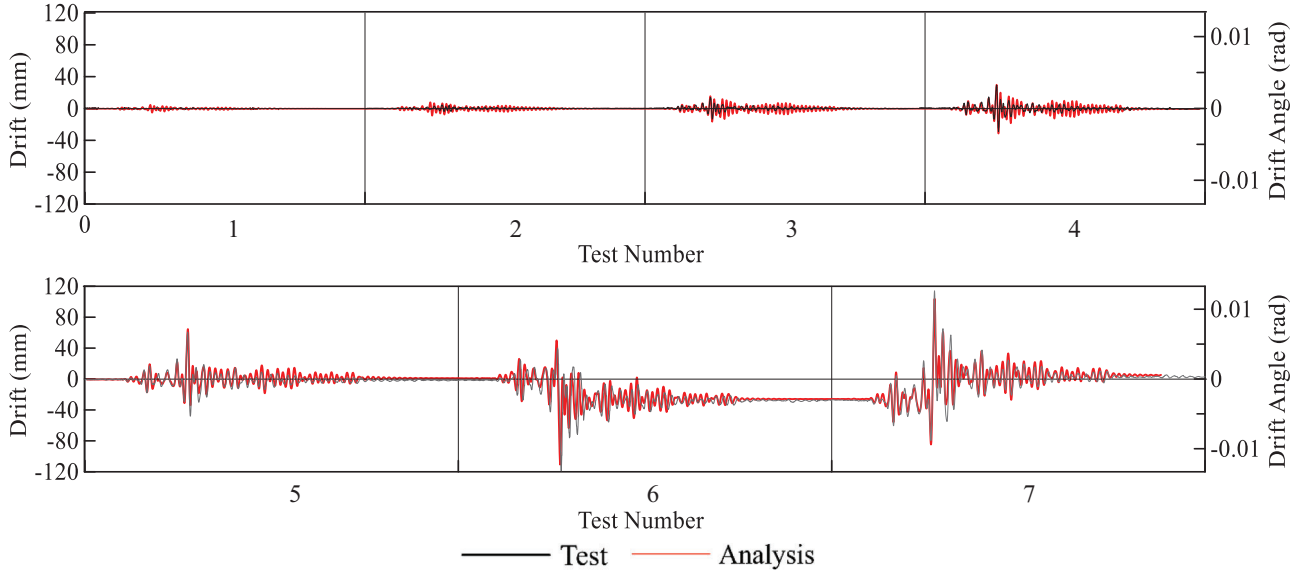


FIGURE 16 | Roof drift response for the test sequence in Phase 1.

10969845, 2025, 3, Downloaded from https://onlinelibrary.wiley.com/doi/10.1002/eqe.4300 by University Of California, Wiley Online Library on [07/11/2026]. See the Terms and Conditions (https://onlinelibrary.wiley.com/terms-and-conditions) on Wiley Online Library for rules of use; OA articles are governed by the applicable Creative Commons License

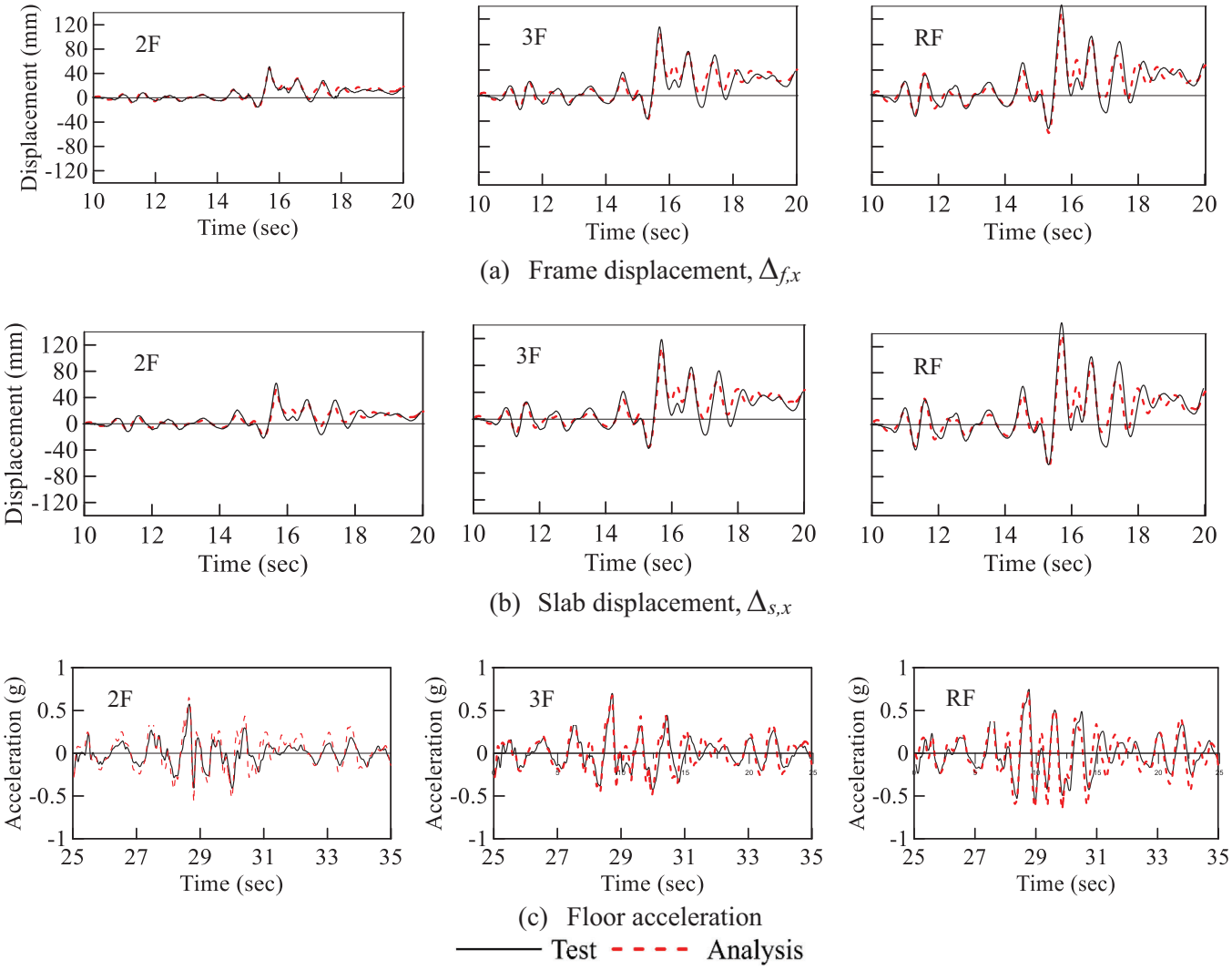


FIGURE 17 | Displacement and floor acceleration histories.

H-SBRB in Section 2.3 and compare the response of the frames with and without sliding slabs. Table 4 lists the 11 motions, six of which were selected from the 1999 Chi-Chi earthquake recorded at different stations. The remaining five motions were earthquakes from around the world, including the 2022 Chihshang motion recorded at the EYUL-EW station in Taitung, Taiwan. The motion spectra were scaled to the DBE level for the Tainan City site according to the Taiwan Seismic Building Code [32], and then factored by 1.3 to scale them to the MCE level (Figure 19). The scaling method used was the amplitude scaling method as specified in Chapter 16 of the ASCE 7–22 code [21]. The scaling period range corresponded to $0.2T_n$ to $2.0T_n$, where T_n is the first mode period of the building specimen ($T_n = 0.52$ s). The lower bound, $0.2T_n$, is required to capture the higher mode response, even though no significant contribution from higher modes was expected for the three-story specimen. The upper bound, $2.0T_n$, is required to account for the period elongation due to possible extensive yielding at the MCE level. The spectra average was scaled until every point exceeded 90% of the code spectra within the period range.

4.2 | Effects of H-SBRB and Sliding Slab on Frame Response

Figure 20 shows the peak relative displacement and H-SBRB deformation of the three-story frame under the 11 near-fault motions at the DBE and MCE levels. At the DBE level, the mean peak relative displacement of the frame (marked by a blue solid circle) was 2.7, 5.1, and 10 mm, and the mean peak H-SBRB deformation (marked by a blue solid rectangle) was 1.4, 3.6, and 7.1 mm at the second, third, and roof floor, respectively. For all the motions, H-SBRB at the second and third floors remained elastic. At the roof, the yield point of the H-SBRB was exceeded in most of the motions. At the MCE level, the mean peak relative displacement of the frame was 3.3, 7.1, and 17.7 mm and the mean peak H-SBRB deformation was 1.7, 5.4, and 14.7 at the second, third, and roof floors, respectively.

The slab sliding increased rapidly at the roof as the H-SBRB reached the post-yield stiffness. The second-floor slab experienced minimal sliding, and the H-SBRB remained within the

10969845, 2025, 3, Downloaded from https://onlinelibrary.wiley.com/doi/10.1002/eqe.4300 by University Of California, Wiley Online Library on [07/11/2026]. See the Terms and Conditions (https://onlinelibrary.wiley.com/terms-and-conditions) on Wiley Online Library for rules of use; OA articles are governed by the applicable Creative Commons License

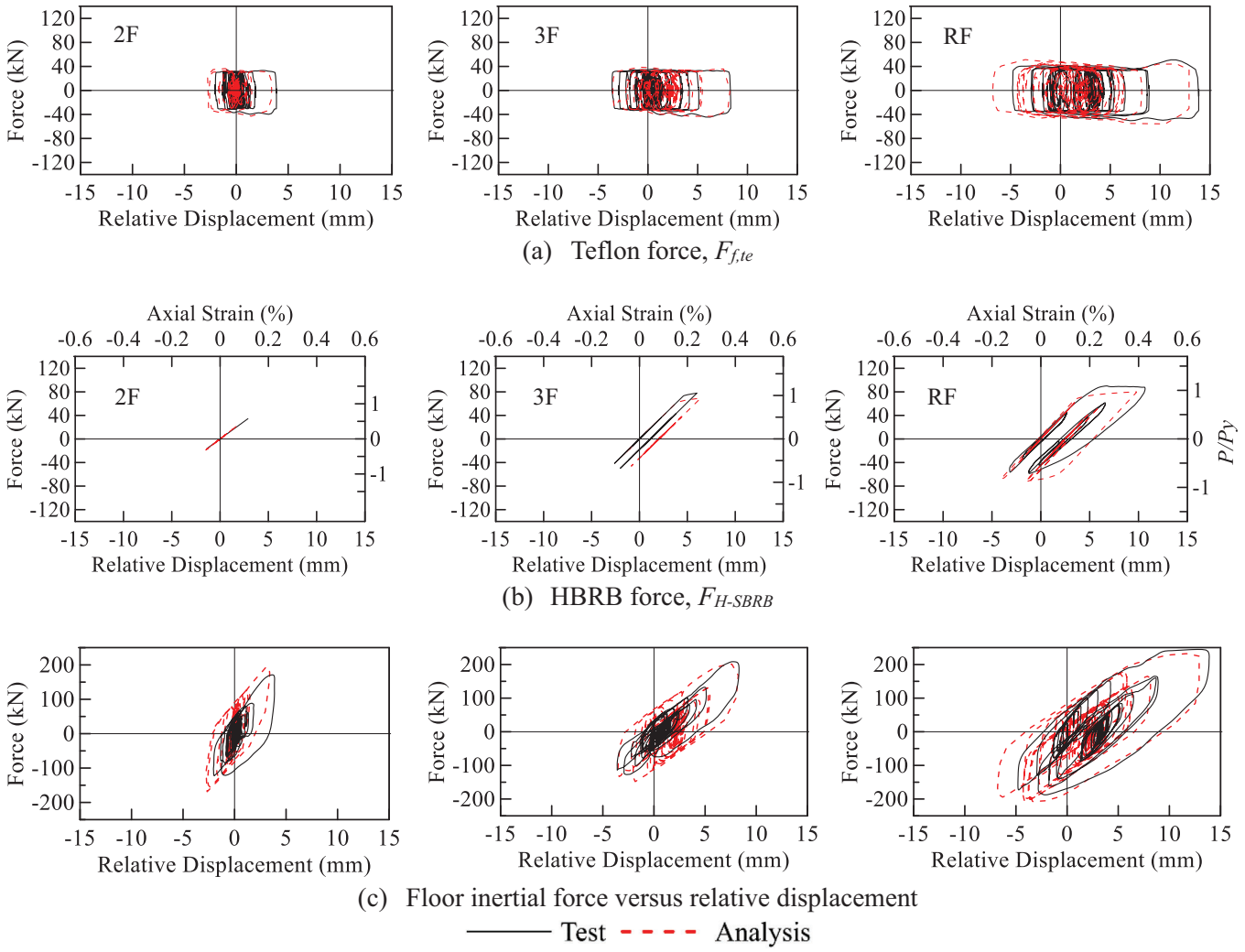


FIGURE 18 | Comparison between test and analysis from the 3D model.

TABLE 4 | Eleven near-fault motions.

No.	Event	Station	PGA (g)	Scale factor (DBE level)	Scale factor (MCE level)
NF1	Chi-Chi, 1999	CHY101-EW	0.34	1.43	1.84
NF2	Chi-Chi, 1999	TCU029-EW	0.16	2.77	3.59
NF3	Chi-Chi, 1999	TCU029-NS	0.20	2.46	3.19
NF4	Chi-Chi, 1999	TCU031-EW	0.11	3.93	5.08
NF5	Chi-Chi, 1999	TCU053-EW	0.23	1.76	2.27
NF6	Chi-Chi, 1999	YCU068-EW	0.51	0.79	1.02
NF7	El Centro, 1940	El Centro-#6-230	0.45	1.27	1.64
NF8	Chihshang, 2022	EYUL-EW	0.37	1.40	1.81
NF9	Northridge-01, 1994	Sta-360	0.59	0.55	0.71
NF10	Kobe, 1995	KJMA-000	0.83	0.47	0.61
NF11	Christchurch, 2011	Pages Road Pumping Sta-EW	0.67	0.84	1.09

10969845, 2025, 3, Downloaded from https://onlinelibrary.wiley.com/doi/10.1002/eqe.4300 by University Of California, Wiley Online Library on [07/11/2026]. See the Terms and Conditions (https://onlinelibrary.wiley.com/terms-and-conditions) on Wiley Online Library for rules of use; OA articles are governed by the applicable Creative Commons License

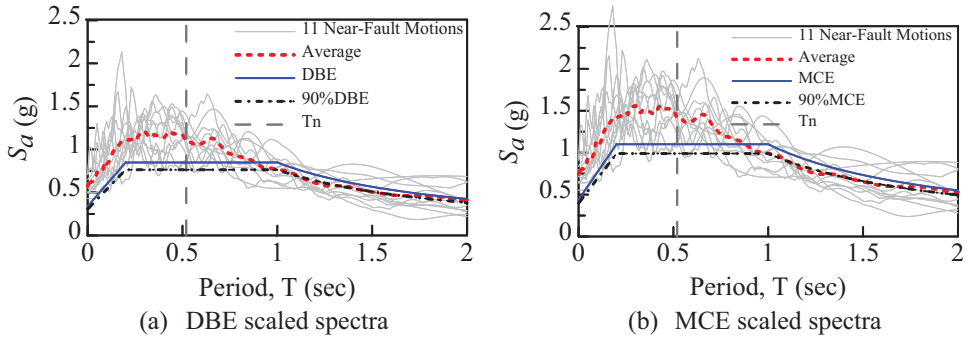


FIGURE 19 | Response spectra for the 11 near-fault motions scaled to the DBE and MCE levels.

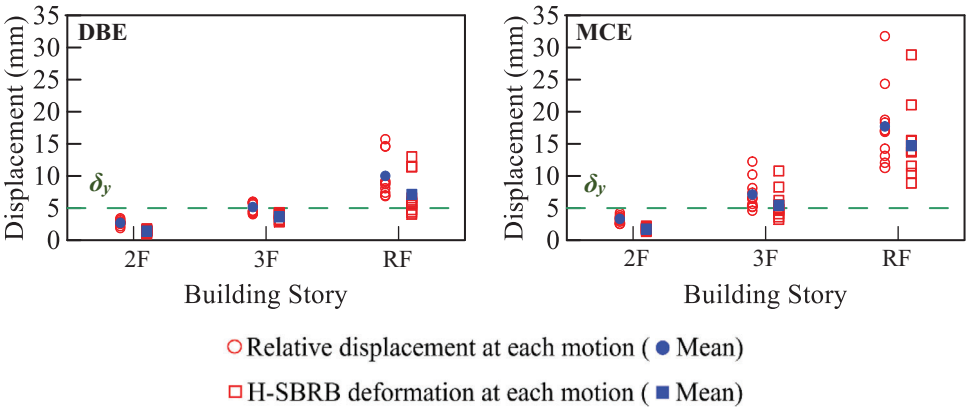


FIGURE 20 | Peak relative displacement and H-SBRB deformation of the frame under 11 near-fault motions.

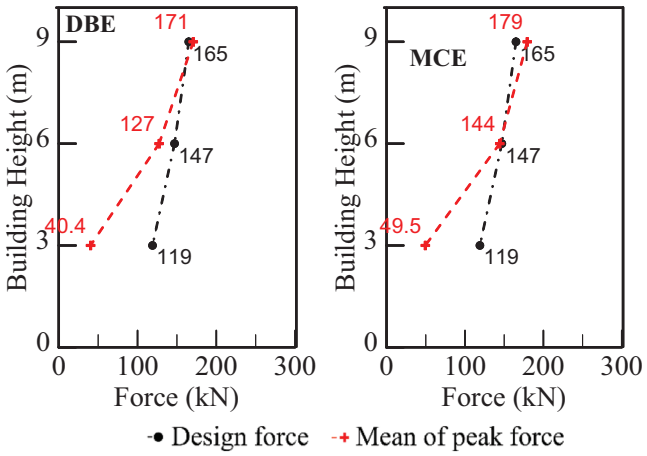


FIGURE 21 | Design force and mean of H-SBRB peak force in 11 near-fault motions.

elastic range, providing a nearly rigid connection between the slab and steel frame. Figure 21 shows the H-SBRB design force and the mean of the H-SBRB peak axial force in all motions. At the DBE level, only the roof reached the design force. At the MCE level, both the third floor and roof reached the design force. The analytical results show the activation of the slab sliding at the roof, at the DBE level, and the second and third floor H-SBRBs remained elastic. At the MCE level, the model shows significant slab sliding at the third floor and roof, with the peak H-SBRB force close to the design force described in Section 2.3.

To compare the sliding slab system with a conventional system where the slab is rigidly connected to the frame, further analyses were conducted on a three-story frame with the rigidly-connected slab at each floor. The 3D three-story frame model was modified by replacing the H-SBRB with a rigid element at each floor. Figure 22 shows the peak floor acceleration and interstory drift angle of the two frames under the 11 motions. In Figure 22A, the reduction of the mean peak floor acceleration was 1.1%, 16.5%, and 9.6% at the DBE level and 7.3%, 19.4%, and 12.1% at the MCE level for the second, third, and roof floors, respectively. A line was added joining the mean values for both the sliding slab (solid line) and rigidly-connected slab (dashed line) models. The model with a rigidly-connected slab depicts a more traditional first-mode controlled distribution, whereas the frame with a sliding slab depicts a constant acceleration at the second and third floors and higher acceleration at the roof floor. However, this constant pattern is a result of the statistical mean, which cancels out extreme values for each motion individually. The peak interstory drift angle of two frames is shown in Figure 22B. The frame with the sliding slab shows a mean reduction of 10.2%, 10.9%, and 15.1% at the DBE level and 10.5%, 11.1%, and 13.4% at the MCE level for the second, third, and roof stories, respectively. The sliding slab can reduce the peak floor acceleration and interstory drift angle of the three-story frame at the DBE and MCE levels.

The inertial force was determined by multiplying the floor acceleration by the floor mass. Figure 23 shows the peak inertial force of the two frames under 11 near-fault motions. The vertical distribution pattern of the inertial force is similar to that of the

10969845, 2025, 3, Downloaded from https://onlinelibrary.wiley.com/doi/10.1002/eqe.4300 by University Of California, Wiley Online Library on [07/11/2026]. See the Terms and Conditions (https://onlinelibrary.wiley.com/terms-and-conditions) on Wiley Online Library for rules of use; OA articles are governed by the applicable Creative Commons License

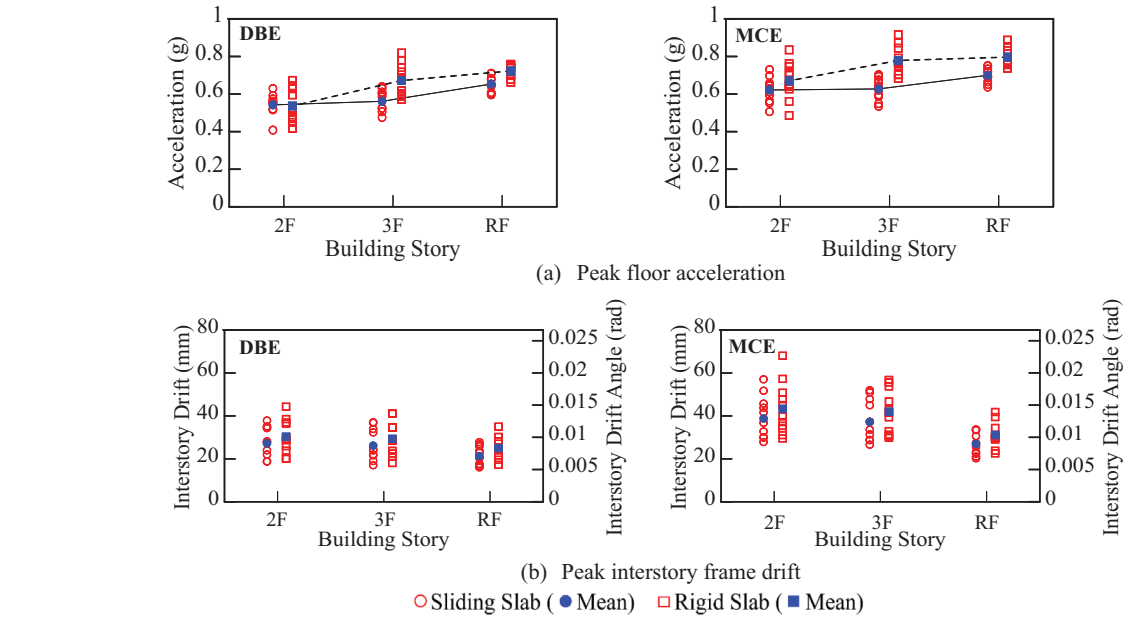


FIGURE 22 | Peak floor acceleration and interstory drift of two frames with sliding slab or rigidly-connected slab.

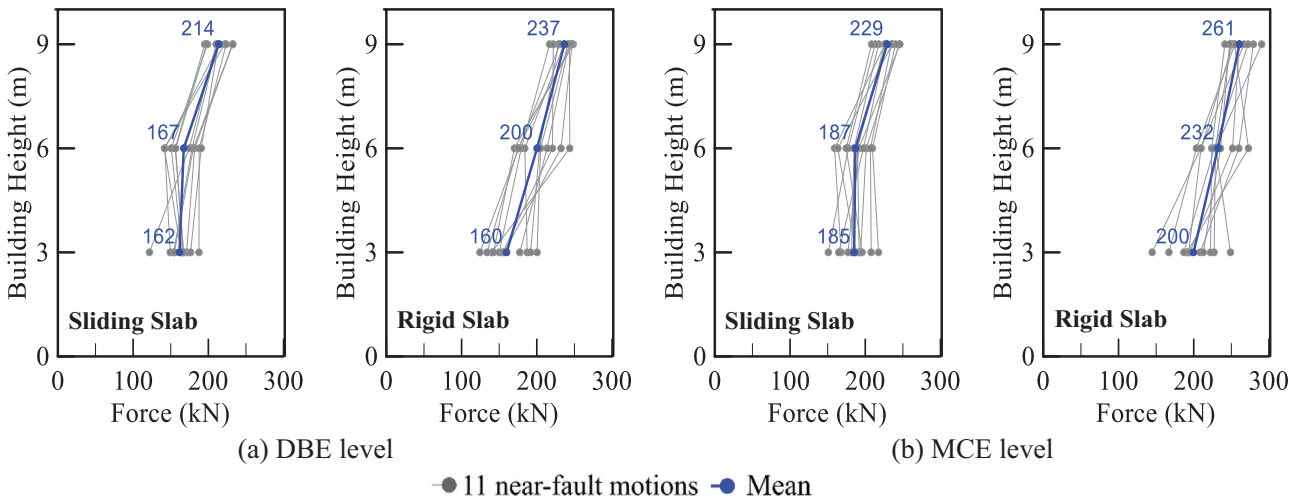


FIGURE 23 | Peak inertial force for the 11 near-fault motions.

floor acceleration, as observed in Figure 22A. Note that the mean peak inertial force was reduced by 10% at the DBE and MCE levels when using the sliding slab in the frame, resulting in a base shear reduction of 9% at the DBE level and 13% at the MCE level.

4.3 | Effect of Different H-SBRB Design Force on Frame Response

The H-SBRB design forces were computed according to the diaphragm force procedure in ASCE 7–22 [21], then magnified by a scale factor of 1.5, as described in Section 2.3 to limit slab sliding before the MCE level. As observed in Section 4.2, the three-story frame model showed limited sliding at the DBE level (Figure 20). To develop more deformation in the horizontal device and more relative displacement at the slab at the DBE level, the H-SBRB design forces could be reduced to the design level, as described in ASCE 7–22 [21]. Therefore, the previous H-SBRB design forces were divided by a factor of 1.5 and the new design values were 79, 98, and 110 kN at the second, third, and roof floors, respectively. The NF6 motion was selected to present the results since it displayed the larger slab sliding response among the six Chi-Chi motions. For simplicity, the initial design force of H-SBRB is referred to as Design 1 and the new design force of H-SBRB is referred to as Design 2.

Figure 24 shows the peak relative displacement and H-SBRB deformation in the three-story frame in the NF6 motion. Except for the second floor, the reduced design force for H-SBRB results in the larger relative displacement between the frame and slab (i.e., slab sliding) and the larger axial deformation of H-SBRB. Significant sliding is observed at the roof at the DBE level and at the third floor and roof at the MCE level because a low post-yield stiffness of the H-SBRB allows for a rapid increase in deformation.

10969845, 2025, 3, Downloaded from https://onlinelibrary.wiley.com/doi/10.1002/eqe.4300 by University Of California, Wiley Online Library on [07/11/2026]. See the Terms and Conditions (https://onlinelibrary.wiley.com/terms-and-conditions) on Wiley Online Library for rules of use; OA articles are governed by the applicable Creative Commons License

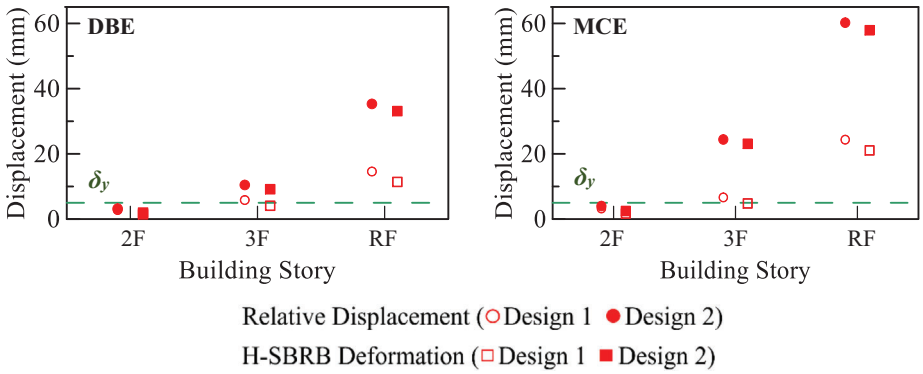


FIGURE 24 | Comparison of the peak relative displacement and H-SBRB deformation based on Design 1 and 2 (NF6 motion).

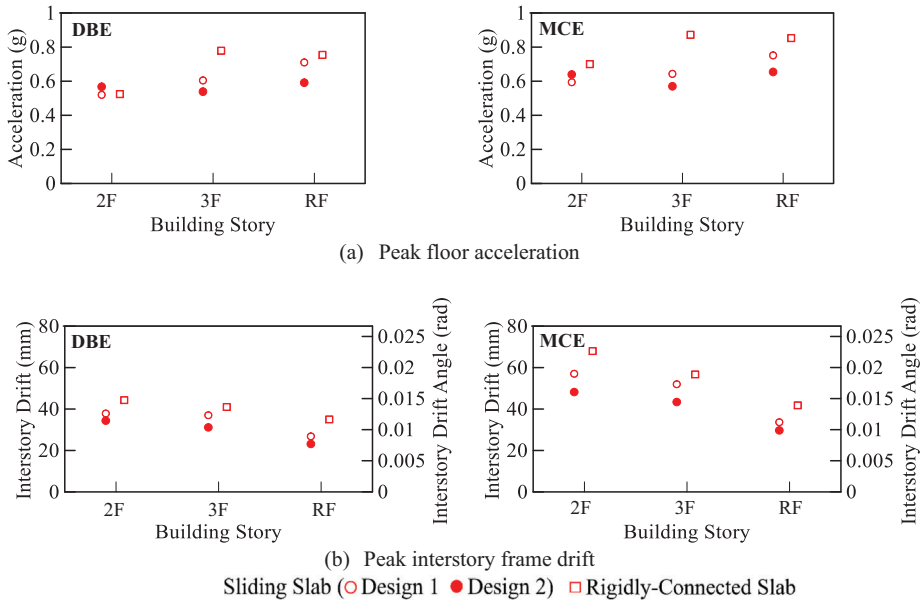


FIGURE 25 | Peak floor acceleration and interstory frame drift between Design 1, Design 2, and the rigidly-connected slab (NF6 motion).

Figure 25 shows the comparison of the three-story frame with the sliding slab, based on two different design forces of H-SBRB (i.e., Design 1 and Design 2), and the frame with the rigidly-connected slab. Except for the second floor, which experienced minor slab sliding at the DBE level, the floor acceleration (Figure 25A) is significantly reduced when transitioning from the rigidly-connected slab to the sliding slab using the ASCE 7–22 [21] design force for H-SBRBs (i.e., Design 2). In Figure 25B, when comparing the Design 2 with the rigidly-connected slab case, the frame interstory drifts are reduced at the DBE level by 22%, 24%, and 34% at the second, third, and roof floors, respectively. A smaller reduction in frame interstory drift is observed when comparing the Design 1 with the rigidly-connected slab case. The largest interstory drift angle occurred at the first floor, where the peak values were 0.015, 0.013, and 0.01 radians for the rigid, Design 1, and Design 2 cases, respectively. The same trend is observed for the three frames at the MCE level.

5 | Conclusions

A three-story dual frame with sliding slab at each floor was tested on a shaking table to study its seismic performance [17]. In this work, a three-dimensional (3D) computer model of the testing frame was constructed using the PISA3D computer program [23]. The analytical model included the definition of beam-column elements with rigid zones at beam-to-column joints and panel zone stiffness (Equation 3). Rotational springs modeled the flexural stiffness of the gravity beam connections, validated from test results (Figure 3). The H-SBRBs, designed based on [18], were modeled incorporating isotropic and kinematic hardening properties, adjusted to fit component test results (Figure 6). The main objectives of the research were to (1) perform a correlation between the analytical 3D model and the experimental results; (2) assess the sliding slab system's effectiveness in mitigating the seismic response by comparing it to a model with rigidly-connected slab; and (3) validate the H-SBRB design forces through nonlinear response-history analyses in multiple ground motions. The conclusions can be drawn below.

1. Tests were conducted to assess the frictional behavior between Teflon and steel interfaces and a velocity-dependence with growing friction coefficient was shown (Figure 10G). The Teflon-to-steel frictional behavior was incorporated in the 3D frame model using a bilinear velocity-dependent element. The unintended friction showed a

10969845, 2025, 3, Downloaded from https://onlinelibrary.wiley.com/doi/10.1002/eqe.4300 by University Of California, Wiley Online Library on [07/11/2026]. See the Terms and Conditions (https://onlinelibrary.wiley.com/terms-and-conditions) on Wiley Online Library for rules of use; OA articles are governed by the applicable Creative Commons License

complex response at low relative displacements and a frictional-type response at larger relative displacements, and was modeled using a truss element adopting a modified Coulomb friction model. The 3D frame model reasonably predicted the test results for the slab and frame displacement, floor acceleration, and overall slab sliding response (test 7), as shown in Figures 16–18.

2. The H-SBRB design forces were computed according to the diaphragm force procedure in ASCE 7–22 [21] and then magnified by a scaling factor of 1.5. By running multiple NRHA, the 3D frame model showed sliding activation in motions at the DBE level, with the H-SBRBs on the second and third floors remaining in the elastic range and the H-SBRB on the roof experiencing minor yielding. At the MCE level, the model showed significant sliding at the roof (17.7 mm), with the second-floor H-SBRB remaining in the elastic range, the H-SBRB on the third floor experiencing minor yielding, and the H-SBRB on the roof undergoing significant yielding (Figure 21).
3. When comparing the sliding slab system to the rigidly-connected slab system at the DBE level, the mean peak floor acceleration was reduced by 16.5% at the third floor (Figure 22A), the interstory drift angle by 15% at the roof (Figure 22B), and the base shear by 9%. When comparing the sliding slab system to the rigidly-connected slab system at the MCE level, the mean peak floor acceleration was reduced by19.4% at the third floor (Figure 22A), the interstory drift angle by 13.4% at the roof (Figure 22B), and the base shear by 13%.
4. The initial H-SBRB design (Design 1) was compared to a different design (Design 2) to increase sliding at the DBE level. The frame based on Design 1 resulted in sliding activation primarily at the roof floor H-SBRBs at the DBE level, barely exceeding the yield point. In contrast, the frame based on Design 2 exceeded the yield point at the third floor and exhibited large inelastic deformations at the roof (Figure 24). This led to a reduction in floor acceleration by 31% (Figure 25A) and interstory drift reduction by 34% (Figure 25B). At the MCE level, more significant reduction in acceleration and interstory drift angle can be observed in the frame with the smaller design force in H-SBRB, as computed based on ASCE 7–22 [21].

Since the study focused on the system under unidirectional loading, future research is needed to investigate the system under bidirectional loading or with an irregular column grid. A regular structural plan and elevation would be a potential archetype for future applications.

Acknowledgments

This work was funded by the National Science and Technology Council under the project number MOST 111-2625-M-002-006, Taiwan and the 2022 Innovative Project of National Applied Research Laboratories.

Data Availability Statement

The data that support the findings of this study are available from the corresponding author upon reasonable request.

References

1. S. Liu and G. P. Warn, "Seismic Performance and Sensitivity of Floor Isolation Systems in Steel Plate Shear Wall Structures," *Engineering Structures* 42 (2012): 115–126.

2. S. Cui, M. Bruneau, and A. Kasalanati, "Seismic Response Case Study of Isolated Floor System Having Special Biaxial Spring Units," *Journal of Structural Engineering* 142, no. 12 (2016): 05016002.

3. Y. Xiang and Y. Koetaka, "Structural Feasibility of Incorporating the LVEM-Isolated Floor in the First Story of a Two-Story Steel Frame," *Engineering Structures* 199 (2019): 109686.

4. Y. Xiang, Y. Koetaka, K. Nishira, et al., "Steel frame with aseismic floor: From the viscoelastic decoupler model to the elastic structural response," *Earthquake Engineering & Structural Dynamics* 50, no. 6 (2021): 1651–1670.

5. H. Anajafi and R. A. Medina, "Robust Design of a Multi-Floor Isolation System," *Structural Control and Health Monitoring* 25, no. 4 (2018): e2130.

6. L. Casagrande, E. Villa, A. Nespoli, A. Occhiuzzi, A. Bonati, and F. Auricchio, "Innovative Dampers as Floor Isolation Systems for Seismically-Retrofit Multi-Storey Critical Facilities," *Engineering Structures* 201 (2019): 109772.

7. R. Villaverde, "Aseismic Roof Isolation System: Feasibility Study With 13-Story Building," *Journal of Structural Engineering* 128, no. 2 (2002): 188–196.

8. R. Villaverde, M. Aguirre, and C. Hamilton (2004). Aseismic Roof Isolation System Built With Steel Oval Dampers. 13th World Conference on Earthquake Engineering, Vancouver, B.C., Canada.

9. J. M. Kelly, R. I. Skinner, and A. J. Heine, "Mechanisms of Energy Absorption in Special Devices for Use in Earthquake Resistant Structures," *Bulletin of the New Zealand Society for Earthquake Engineering* 5, no. 3 (1972): 63–88.

10. R. I. Skinner, J. M. Kelly, and A. J. Heine, "Hysteretic Dampers for Earthquake-Resistant Structures," *Earthquake Engineering & Structural Dynamics* 3, no. 3 (1974): 287–296.

11. G. Tsampras, R. Sause, D. Zhang, et al., "Development of Deformable Connection for Earthquake-Resistant Buildings to Reduce Floor Accelerations and Force Responses," *Earthquake Engineering & Structural Dynamics* 45, no. 9 (2016): 1473–1494.

12. G. Tsampras, *Force-Limiting Deformable Connections for Earthquake Resistant Buildings* (Dept. Civil and Environmental Engineering, Lehigh University, Bethlehem, PA, 2016). PhD Dissertation.

13. G. Tsampras, R. Sause, R. B. Fleischman, and J. I. Restrepo, "Experimental Study of Deformable Connection Consisting of Buckling-Restrained Brace and Rubber Bearings to Connect Floor System to Lateral Force-Resisting System," *Earthquake Engineering & Structural Dynamics* 46, no. 8 (2017): 1287–1305.

14. G. Tsampras, R. Sause, R. B. Fleischman, and J. I. Restrepo, "Experimental Study of Deformable Connection Consisting of Friction Device and Rubber Bearings to Connect Floor System to Lateral Force-Resisting System," *Earthquake Engineering & Structural Dynamics* 47, no. 4 (2018): 1032–1053.

15. Z. Zhang, R. B. Fleischman, J. I. Restrepo, et al., "Shake-Table Test Performance of an Inertial Force-Limiting Floor Anchorage System," *Earthquake Engineering & Structural Dynamics* 47, no. 10 (2018): 1987–2011.

16. M. Paronesso and D. G. Lignos, "Seismic Design and Performance of Steel Concentrically Braced Frame Buildings With Dissipative Floor Connectors," *Earthquake Engineering & Structural Dynamics* 51, no. 15 (2022): 3505–3525.

17. C. C. Chou, H. Z. Lin, A. Córdova, et al., "Earthquake Simulator Testing of a Three-Story Steel Building for Evaluating Built-Up Box Column Performance and Effect of Sliding Slab," *Earthquake Engineering and Structural Dynamics* 53, no. 9 (2024): 2637–2655, https://doi.org/10.1002/eqe.4130.

10969845, 2025, 3, Downloaded from https://onlinelibrary.wiley.com/doi/10.1002/eqe.4300 by University Of California, Wiley Online Library on [07/11/2026]. See the Terms and Conditions (https://onlinelibrary.wiley.com/terms-and-conditions) on Wiley Online Library for rules of use; OA articles are governed by the applicable Creative Commons License

18. C. C. Chou and S. Y. Chen, "Subassemblage Tests and Finite Element Analyses of Sandwiched Buckling-Restrained Braces," *Engineering Structures* 32, no. 8 (2010): 2108–2121.

19. ANSI/AISC 360-22, *Specification for Structural Steel Buildings* (Chicago, Illinois: American Institute of Steel Construction, 2022).

20. C. M. Lin, Y. W. Chang, C. C. Chou, et al., "Reconnaissance of the 2022 Guanshan and Chihshang Earthquakes in Eastern Taiwan." *Earthquake Spectra* 40, no. 1 (2023): 531–565, https://doi.org/10.1177/87552930231209102.

21. ASCE/SEI 7–22, *Minimum Design Loads and Associated Criteria for Buildings and Other Structures* (American Society of Civil Engineers, Reston, VA 2022).

22. O. A. Lopez and M. Cruz, "Number of Modes for the Seismic Design of Buildings," *Earthquake Engineering & Structural Dynamics* 25, no. 8 (1996): 837–855.

23. B. Z. Lin, Y. J. Yu, M. C. Chuang, and K. C. Tsai, *Platform of Inelastic Structural Analysis for 3D Systems, PISA3D. Standard Edition R3.2, User's Manual*, (National Center for Research on Earthquake Engineering, Taiwan. Dept. of Civil Engineering, National Taiwan University, Taipei, Taiwan, 2011).

24. C. C. Chou, J. H. Liu, and D. H. Pham, "Steel Buckling-Restrained Braced Frames With Single and Dual Corner Gusset Connections: Seismic Tests and Analyses," *Earthquake Engineering and Structural Dynamics* 41, no. 41 (2012): 1137–1156.

25. H. Krawinkler, "Shear in Beam-Column Joints in Seismic Design of Steel Frames," *Engineering Journal* 15, no. 3 (1978): 82–91.

26. AISC, *Seismic Provisions for Structural Steel Buildings, ANSI/AISC 341-22* (Chicago, Illinois: American Institute of Steel Construction, 2022).

27. J. M. Chen, *One-story Steel Frame Tests Using a Stiffness Adjustable Self-centering Brace and Sandwiched Buckling-restrained Brace, Thesis Advisor: Chou, C. C*. (Dept. of Civil Engineering, National Taiwan University, Taipei, Taiwan. (in Chinese), 2023).

28. C. J. Wu, *Shaking Table Tests of a Novel Full-scale Three-story Steel Self-centering Braced Frame With Sliding Slabs, Thesis Advisor: Chou, C. C*. (Dept. of Civil Engineering, National Taiwan University, Taipei, Taiwan. (in Chinese), 2024).

29. A. Mokha, M. Constantinou, and A. Reinhorn, "Teflon Bearings in Base Isolation I: Testing," *Journal of Structural Engineering* 116, no. 2 (1990): 438–454.

30. D. Fluoroproducts, Teflon® ptfe fluoropolymer resin: properties handbook. DuPont Fluoroproducts: Wilmington, NC, USA (1996).

31. M. Constantinou, A. Mokha, and A. Reinhorn, "Teflon Bearings in Base Isolation II: Modeling," *Journal of Structural Engineering* 116, no. 2 (1990): 455–474.

32. Taiwan Code *Design and Technique Specifications of Steel Structures for Buildings* (Construction and Planning Agency, Ministry of the Interior, Taipei, Taiwan 2010).

33. Y. T. Huang, D. Y. H. Chou, C. C. Chou, and C. H. Loh, "Data-Driven Structural Health Monitoring on Shaking Table Tests of a 3-Story Steel Building With Sliding Slabs," *Structural Control and Health Monitoring* 2024, no. 1 (2024): 3412305.

10969845, 2025, 3, Downloaded from https://onlinelibrary.wiley.com/doi/10.1002/eqe.4300 by University Of California, Wiley Online Library on [07/11/2026]. See the Terms and Conditions (https://onlinelibrary.wiley.com/terms-and-conditions) on Wiley Online Library for rules of use; OA articles are governed by the applicable Creative Commons License